

# Multi-scale analysis of shear behaviour of crushable granular sand under general stress conditions

KE SHI\*, FAN ZHU† and JIDONG ZHAO‡

Grain crushing underpins key mechanical behaviours of granular materials. A variety of factors, including grading, particle shapes and loading conditions, have been recognised to affect the crushability of grains and the overall behaviour of a granular material. Among them, the role of intermediate principal stress in a general stress condition on the shear behaviour of crushable granular sand remains less understood, owing to the scarcity of experimental data and analytical tools available. In this paper, a multi-scale computational approach is employed to investigate the shear behaviour of crushable granular sand under general stress conditions with varying intermediate principal stresses and confining pressures. The computational approach features multi-scale coupling between non-smooth contact dynamics and peridynamics, and offers a rigorous way to consider the intertwined evolution of particle size and shape during the process of grain crushing. The numerical study helps to quantify comprehensively and analyse the grain crushing-induced changes of macro- and micro-scale material behaviours including strength, deformability, particle size and shape evolution, particle-scale forces and contact conditions, and the development of anisotropy. The competition between a void-filling mechanism due to grain size change and enhanced friction and interlocking due to grain shape change in dictating the deformation of crushable sand is further discussed. The findings offer insights into the complex behaviours of crushable granular materials under general stress conditions and facilitate future development of physics-based constitutive theories on crushable sand.

**KEYWORDS:** contact dynamics; fabric/structure of soils; grain crushing; granular materials; intermediate principal stress ratio; multi-scale modelling; particle crushing/crushability; peridynamics

## INTRODUCTION

Grain crushing underpins the mechanical responses of granular materials. The crushing of grain may lead to continuous evolution of particle size and shape (Lade *et al.*, 1996; Köken, 2020) in a granular assembly, resulting in constant changes of the engineering properties of a granular material. Understanding the mechanisms of grain crushing and their effect on mechanical material properties is critical for proper assessment of the performance of granular media pertaining to many engineering fields and industries, including geotechnical, mining and chemical engineering, and the pharmaceutical industry, where granular materials are routinely handled. For geomaterials such as sand, their engineering properties, including strength, deformation, critical state behaviour and failure, are all affected by grain crushability (Lade *et al.*, 1996; Bandini & Coop, 2011; Yu, 2017a). In the mining industry, the comminution process of rock aggregates accomplished by impactors and crushers is of great importance (Köken, 2020). A clear understanding of the crushing mechanism based upon reliable simulation of the grain breakage processes is vital to the design of those crushers with optimum energy consumption.

In view of its strong engineering and industrial relevance, the behaviour of crushable granular materials has been extensively investigated by means of experimental, numerical and theoretical approaches. On a single particle level, diametric compression tests have been routinely performed on glass beads or silica sand (McDowell, 2002; Zhao *et al.*, 2015) to study the fracture patterns and particle strength under uniaxial loading conditions. On the macroscopic scale, the responses of crushable granular materials are often studied using conventional triaxial tests with designated radial confining pressures. Suppressed dilation and grading evolution towards a fractal distribution have been observed in crushable sand under shearing or compression (Miao & Airey, 2013; Jia *et al.*, 2017; Yu, 2017b). Recent use of X-ray tomography enables rigorous examination of the effect of grain morphology and coordination number on the breakage mode and the yielding of granular materials (Karatzas *et al.*, 2019). Based on those experimental results, various failure criteria and indices have been proposed to quantify the degree of breakage and have been incorporated into constitutive models to predict the mechanical behaviours of granular materials (Lobo-Guerrero & Vallejo, 2005; McDowell & de Bono, 2013; Hanley *et al.*, 2015). Numerical investigations on the topic, based on popular methods such as the discrete-element method (DEM), offer an economic option for probing the internal structure of granular materials under designated loads. The convenient track of particle size distribution (PSD) evolution and precise control of loading conditions in numerical simulations provide an idealised environment to study grain crushing (Wang & Yan, 2013; Ciantia *et al.*, 2015; Nguyen *et al.*, 2018). Comprehensive studies on the micromechanics of crushable granular materials under various stress conditions have revealed the significance of the initial fabric structure to macroscopic crushing behaviour (De Bono & McDowell,

Manuscript received 21 December 2021; revised manuscript accepted 5 July 2022. First published online ahead of print 3 October 2022.

Discussion on this paper closes on 1 September 2024, for further details see p. ii.

\* Hong Kong University of Science and Technology, Hong Kong, P. R. China.

† Kyoto University, Kyoto, Japan; formerly Hong Kong University of Science and Technology, Hong Kong, P. R. China (Orcid:0000-0001-9922-2225).

‡ Hong Kong University of Science and Technology, Hong Kong, P. R. China (Orcid:0000-0002-6344-638X).

2018; Ciantia *et al.*, 2019). However, the difficulty of reconciling computational efficiency with a realistic description of child particle morphology hinders accurate numerical simulation of crushable granular media with reasonable specimen size.

Existing studies indicate that the crushability of individual particles and the overall mechanical behaviour of crushable granular materials are associated with both external factors (stress state, loading path) and inherent material properties (initial density, grading and shape) (Wang & Yan, 2012; Yu, 2017a, 2017b, 2017c). Nevertheless, earlier experimental tests have mostly been performed under biaxial or traditional loading conditions where the influence of intermediate principal stress is not considered. The simple loading path and axisymmetric stress conditions are inadequate to match with complex engineering scenarios. For example, the construction and impounding of dams are commonly under highly anisotropic loading conditions under which the occurrence of continuous grain crushing and the consequent particle rearrangement and interlocking may negatively affect the long-term settlement and lateral displacement. Therefore, true triaxial testing conditions capable of differentiating the intermediate and minor principal stresses are preferred to examine the behaviour of crushable granular materials under more generalised stress states (Kwasniewski *et al.*, 2012). True triaxial tests conducted on non-crushable granular materials in both laboratories and according to numerical simulations help to unveil the role of intermediate principal stress: the angle of shearing resistance  $\phi_m = \sin^{-1}[(\sigma_1 - \sigma_3)/(\sigma_1 + \sigma_3)]$  exhibits a non-monotonic trend with intermediate principal stress ratio  $b = (\sigma_2 - \sigma_3)/(\sigma_1 - \sigma_3)$  (Wang & Lade, 2001; Sazzad & Suzuki, 2013; Huang *et al.*, 2014a; Xiao *et al.*, 2016). However, the combined effect of intermediate principal stress ratio  $b$  and particle crushing on the mechanical response of granular materials has not been thoroughly investigated. Some recent studies have suggested that particle breakage is indeed affected by intermediate principal stress (Xiao *et al.*, 2014; Zhou *et al.*, 2015). Numerical simulations using DEM have also been performed on sand samples to study the influence of  $b$  on sample crushability and energy input (Liu *et al.*, 2017). Nevertheless, due to experimental limitations, all reported tests have been terminated at relatively small strain levels, barring systematic studies of the profile of particle crushability, sample deformability, grading and shape evolution at large strains. There are also numerical challenges in simulating considerable and sustained breakage events with a realistic consideration of crushing patterns. It is interesting but challenging to examine the evolution of a microscopic fabric network and its correlation with shear strength and anisotropy under various intermediate principal stress conditions.

This paper presents a systematic computational investigation on the macro- and micro-scopic behaviours of crushable granular sand under general stress conditions. The study employs a novel multi-scale computational approach which features the use of non-smooth contact dynamics (NSCD) in the simulation of large-scale discrete granular systems under true triaxial conditions and the employment of peridynamics (PD) in modelling individual particle breakage (Zhu & Zhao, 2019a, 2019b). Both the size and shape of the fragments are reasonably preserved in the simulation with minimal assumptions. Based on the results, the macroscopic behaviours of granular sand in consideration of gain crushing under varying intermediate stresses are examined to investigate the role of breakage and intermediate principal stress in the evolution of soil fabric and shear strength. The aim is to decipher the correlation between the intricate micro-mechanisms of grain crushing and the

strength and deformation behaviour of crushable granular media. The statistical observations characterising unique features of crushing patterns may contribute to the establishment of more comprehensive constitutive theories to model crushable granular media.

## METHODOLOGY

### Peridynamics

The coupling scheme employs the PD method to simulate the breakage of individual sand particles. PD is a non-local mesh-free method originally developed to model discontinuities in the continuum field. The method is based on integration operations of the displacement field rather than the conventional partial differentiation of the displacement field in classical continuum methods such as the finite-element method (FEM), which encounters difficulties when dealing with discontinuities. In PD, a solid material is modelled by discretised material points connected through breakable bonds. Successive breakage of bonds forms fracture surfaces. This feature lends PD an advantage to model problems involving discontinuities and fractures over conventional approaches. Indeed, an increasing number of PD-based studies have recently been reported in simulating the fracture of brittle materials such as ceramics, glass and rocks. In this study, the ordinary state-based PD (Silling *et al.*, 2007) for elastic and isotropic materials is adopted and its basic equation writes

$$\rho(\mathbf{x})\ddot{\mathbf{u}}(\mathbf{x}, t) = \int_{\Omega_x} [\mathbf{T}(\mathbf{x}, t)\langle \mathbf{x}' - \mathbf{x} \rangle - \mathbf{T}(\mathbf{x}', t)\langle \mathbf{x} - \mathbf{x}' \rangle] dV_{x'} + \mathbf{b}(\mathbf{x}, t) \quad (1)$$

where  $\rho(\mathbf{x})$  denotes the material density at point  $\mathbf{x}$ ;  $\mathbf{u}(\mathbf{x}, t)$ ,  $\mathbf{T}(\mathbf{x}, t)$  and  $\mathbf{b}(\mathbf{x}, t)$  refer to the displacement, force state and body force density of material point  $\mathbf{x}$  at time  $t$ , respectively;  $\Omega_x$  represents the set of neighbouring material points interacting with  $\mathbf{x}$ ; and  $V_{x'}$  denotes the volume of a neighbouring material point  $\mathbf{x}'$ .

The breakage of peridynamic bonds is governed by the critical stretch damage model where a bond is considered broken if it is stretched to reach a critical strain  $s_c$  (Madenci & Oterkus, 2014) given by

$$s_c = \sqrt{\frac{G_c}{\left\{3S + (3/4)^4[K - (5S/3)]\right\}}\delta} \quad (2)$$

where  $\delta$  denotes the horizon; and  $S$  and  $K$  represent shear and bulk modulus, respectively. In the present study, the horizon is a radius that defines the extent of the neighbourhood of a material point.  $G_c$  refers to the critical energy release rate which is a material constant that can be measured from experiments.

In the simulation of particle breakage, the strength of a particle is controlled by the  $G_c$  assigned to the material. The characteristic strength of a particle is known to be proportional to the square root of  $G_c$  under uniaxial loading (Zhu & Zhao, 2019a). Given a statistical distribution of the particle strength following a Weibull distribution, a unique value of  $G_c$  is assigned to each particle in the initial packing following

$$G_c = G_{c0}[-\ln(U(0, 1))]^{2/\psi} \left(\frac{V}{V_0}\right)^{-2/\psi} \quad (3)$$

where  $G_c$  and  $G_{c0}$  refer to the critical energy release rate of particles with volume  $V$  and  $V_0$ , respectively;  $\psi$  represents the

Weibull modulus, which is assumed to be 3.0 based on single particle crushing test data (Nakata *et al.*, 2001). In the present study, a base case is defined with  $G_{c0} = 30 \text{ J/m}^2$  for a spherical particle with diameter of 1.7 mm. This gives a characteristic strength of 30 MPa for the particle, which falls within the typical strength range of sand particles (Nakata *et al.*, 2001). For the fragmented particles (which are referred to as child particles), the size effect on particle strength must be considered. In other words, small particles are expected to be stronger than large particles owing to fewer micro-defects being contained (Nakata *et al.*, 1999, 2001). Therefore, at each breakage event, the  $G_c$  of child particles is reassigned by

$$G_{ch} = G_{pr} \left( \frac{V_{ch}}{V_{pr}} \right)^{-2/\psi} \quad (4)$$

where  $G_{ch/pr}$  and  $V_{ch/pr}$  refer to the critical energy release rate and volume of child and parent particle, respectively.

#### Non-smooth contact dynamics

The NSCD is a complementary-based iterative approach (Jean, 1999) developed as an alternative to traditional discrete modelling techniques such as DEM. In NSCD, particles are modelled as rigid bodies with no penetration between contacting pairs, and particle motion is updated based on impulse and velocity rather than force and acceleration. The NSCD is considered advantageous in handling large granular systems composed of irregular-shaped particles, owing to its strong numerical stability and better computational efficiency because large time steps can be adopted (Servin *et al.*, 2014), while the complex particle shapes do not impose extra difficulties in solving the contact forces. The NSCD modelling of a granular system contains three major components: collision detection; differential variational inequality (DVI) discretisation; and time integration. Collision detection is performed through an efficient two-phase algorithm: a broad phase identifies potential collide through an AABB algorithm (Kopta *et al.*, 2012), then a precise narrow phase obtains the contact position and orientation with a GJK algorithm (Van Den Bergen, 2003). All the contacts satisfy the complementarity condition expressed by

$$0 \leq \phi_i(\mathbf{q}) \perp \gamma_{i,n} \geq 0 \quad (5)$$

where  $\phi_i(\mathbf{q})$  and  $\gamma_{i,n}$  refer to the distance and normal contact force between colliding bodies of contact  $i$ , respectively;  $\mathbf{q}$  represents the generalised coordinates of the two bodies. The notation  $\perp$  denotes the orthogonal relation between  $\phi_i(\mathbf{q})$  and  $\gamma_{i,n}$  (that means their inner product is zero). This complementarity condition implies that when two bodies are not in contact ( $\phi_i(\mathbf{q}) > 0$ ), no contact force exists ( $\gamma_{i,n} = 0$ ) and when the contact force is non-zero ( $\gamma_{i,n} > 0$ ), they must be in contact ( $\phi_i(\mathbf{q}) = 0$ ). The equation also requires no penetration between contacting bodies as the contact distance is always non-negative.

The contact constraint model is coupled with the Coulomb friction law in formulating the general equations of motion as DVI (Anitescu & Tasora, 2010). The equations of motion, including particle position, velocity and inter-particle contact forces are formulated based on Newton's second law

$$\mathbf{M}\dot{\mathbf{v}} = \mathbf{f}(\mathbf{q}, \mathbf{v}, t) + \mathbf{g}_q(\mathbf{q}, t) + \sum_{i \in \mathcal{A}} (\gamma_{i,n} \mathbf{D}_{i,n} + \gamma_{i,u} \mathbf{D}_{i,u} + \gamma_{i,w} \mathbf{D}_{i,w}) \quad (6)$$

where  $\mathbf{M}$  and  $\mathbf{v}$  denote the mass and velocity of the objects in contact and the derivative of object position  $\dot{\mathbf{q}}$  is updated through a linear transformation matrix with  $\mathbf{v}$ ;  $\mathbf{f}(\mathbf{q}, \mathbf{v}, t)$  and

$\mathbf{g}_q(\mathbf{q}, t)$  refer to the external force and constraint force in the system;  $\mathbf{D}_{i,n}$ ,  $\mathbf{D}_{i,u}$  and  $\mathbf{D}_{i,w}$  represent the contact normal vector and two tangential vectors, respectively.  $\gamma_{i,n}$ ,  $\gamma_{i,u}$  and  $\gamma_{i,w}$  are the  $i$ th frictional contact force. The DVI is further relaxed to a CCP (cone complementary problem) and solved iteratively. In this study, the widely used Gauss-Seidel-based iterative solver with successive over-relaxation (SOR) is employed. The state of the discrete system is updated through the Euler semi-implicit linearised time-integration scheme, which offers remarkable computational efficiency and strong numerical stability. Validation and applications of the NSCD in simulating geotechnical problems can be found in some recent studies (Kleinert *et al.*, 2013; Izadi & Bezuijen, 2018).

#### Coupling of PD and NSCD methods

The PD and NSCD are coupled to form a multi-scale computational framework, which consists of two major ingredients: first, the PD is used for single particle crushing analysis and, second, the NSCD is employed for modelling the entire discrete granular system. A detailed coupling scheme is illustrated in Fig. 1 and explained in the following.

- All the particles in the granular sample are screened at selected time steps to collect particles that are likely to break. Only those selected particles will be analysed for breakage. The screening is conducted with a constant interval of every 600 time steps, as a balanced consideration between computational efficiency and simulation accuracy. A large interval offers a benefit in terms of the computational cost, but it may not realistically capture the force redistribution (and the resulting particle crushing) immediately after crushing of a particle, whereas a small interval does the opposite. This screening is performed by checking the maximum contact force on a particle against a pre-defined threshold. The maximum contact force criterion has been adopted based on previous studies showing that the crushing probability of a single particle has a strong correlation with the maximum contact force acting on it (Hurley *et al.*, 2018; Zhu & Zhao, 2019b). To capture the crushing events as much as possible, the screening force threshold is conservatively set at 20% lower than the estimated crushing force of the particle under uniaxial loads. The selected particles are further modelled with PD for breakage analysis.
- In PD analysis, each particle is discretised into approximately 3000 material points based on an element size of  $0.055d$ , where  $d$  is the equivalent particle diameter. This stage of breakage analysis is implemented with *OpenMP* multi-threading to enhance computational efficiency.
- If a particle is found to be broken after the breakage analysis, the particle will be replaced by several child particles described by convex or concave polyhedrons. In view of the time-consuming process of contact detection for concave particles, particles with convexity larger than 0.85 or equivalent diameter smaller than 1.0 mm are assumed to be convex for numerical simplification. Doing so may sacrifice the simulation accuracy in terms of particle shape but still offer a reasonable overall mechanical response, as sand particles are mostly convex. In the present study, the aim is to model a quasi-static shearing process of sand. As such, the child particles are assumed not to inherit any kinetic energy from their parent particles, in consideration that the kinetic energy can be quickly dissipated to reach a quasi-static condition for the granular system (Luding *et al.*, 1994).

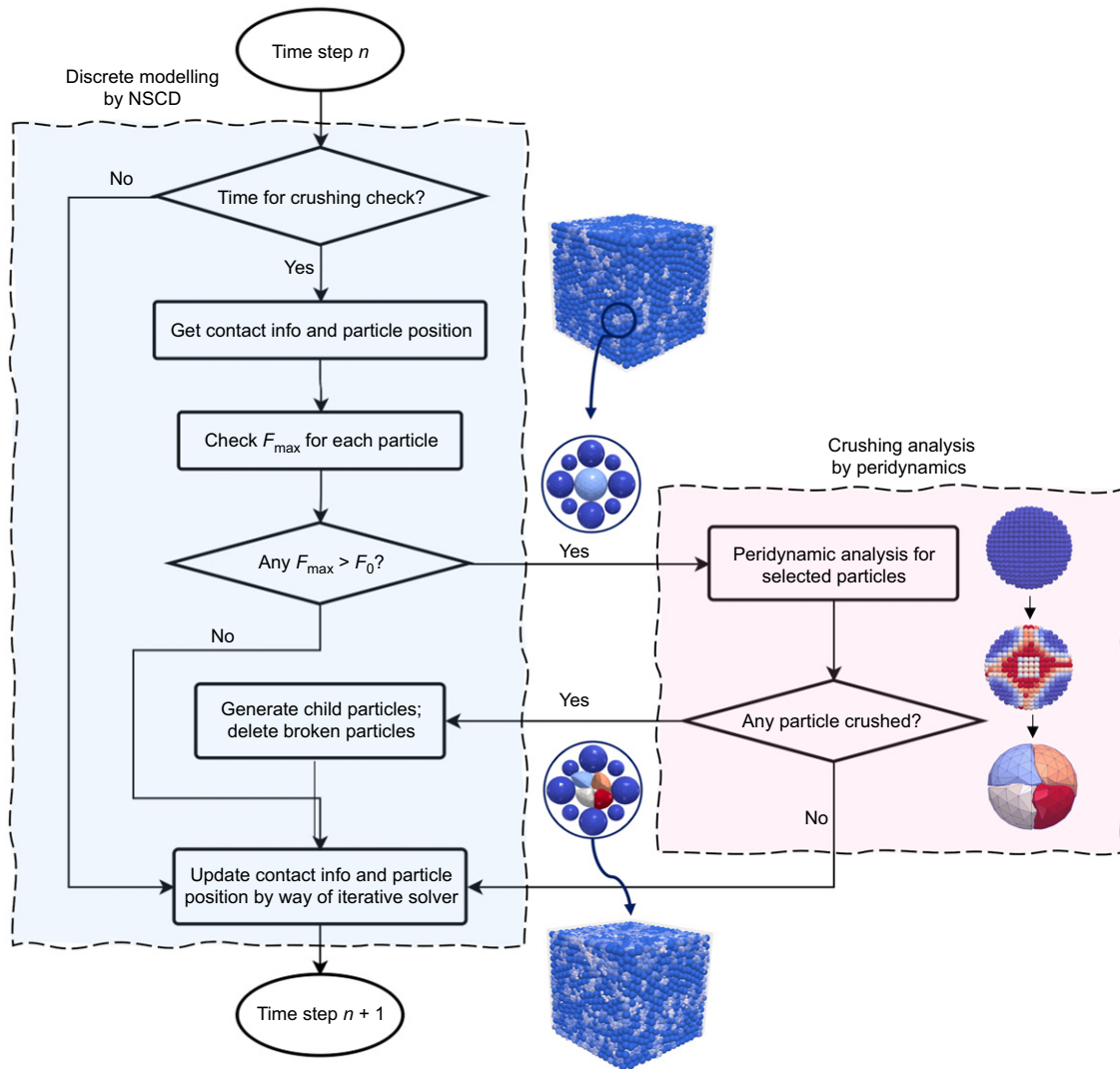


Fig. 1. Workflow for the coupled contact dynamics and peridynamics (PD) approach

The open-source software *Peridigm* (Parks *et al.*, 2012) was employed for the PD analysis and the open-source software *Project Chrono* (Tasora *et al.*, 2015) for the NSCD analysis. All simulation results are visualised by the software *Paraview* in conjunction with *CGAL* to provide geometric representations of convex particles (Fabri & Pion, 2009). The capability of the methodology to model crushable granular materials has been validated by simulation of the one-dimensional (1D) compression of crushable sand (Zhu & Zhao, 2019a, 2021a, 2021b).

#### SIMULATION OF TRUE TRIAXIAL SHEAR ON SAND

To simulate the true triaxial shear of crushable granular sand, numerical specimens are prepared to contain an initial 5000 spherical particles with 1.0 mm dia. randomly packed inside a  $16 \times 16$  mm rigid frictionless container. Mono-dispersed packings are generated here with the purpose of maximising the effect of particle breakage during the shearing process. The relatively small number of initial particles is a trade-off between the simulation accuracy and computational efficiency, as the total number of particles has exceeded 80 000 at the end of shearing in the case with the most significant particle crushing. Each initial packing is

isotropically consolidated to a designated confining pressure. Three confining pressures of 1.5 MPa, 6 MPa and 12 MPa are examined in this study. The consolidated specimens are subjected to further shearing along the vertical direction ( $z$ -axis) to large axial strains with a constant velocity of 0.05 m/s applied on the top platen, as shown in Fig. 2. The ratio of specimen size  $H$  to the largest particle diameter  $d_{\max}$  before and at the end of shearing is 16.4 and 9.6, respectively, which satisfies the minimal specimen size requirement  $H/d_{\max} > 6$  suggested by ASTM D7181 (ASTM, 2011). The loading rate is selected to be sufficiently slow to ensure the quasi-static loading condition by satisfying a threshold of low inertia number  $I_m$  (Perez *et al.*, 2016)

$$I_m = \dot{\epsilon}_1 \frac{d}{\sqrt{p_0/\rho}} = 2.5 \times 10^{-4} - 7.2 \times 10^{-4} < 2.5 \times 10^{-3} \quad (7)$$

where  $\dot{\epsilon}_1$  refers to the axial strain rate, which equals  $4.41 \text{ s}^{-1}$  (equivalent to a shear rate of 0.05 m/s);  $p_0$  is the confining pressure ranging from 1.5 to 12 MPa;  $d$  is the average diameter of the simulated particles, where we conservatively use the maximum particle diameter of 1.0 mm; and  $\rho$  is the particle density, taken to be  $79\,500 \text{ kg/m}^3$ , which is magnified as stated later. The calculated inertia number in equation (7) is thus well below the suggested threshold.

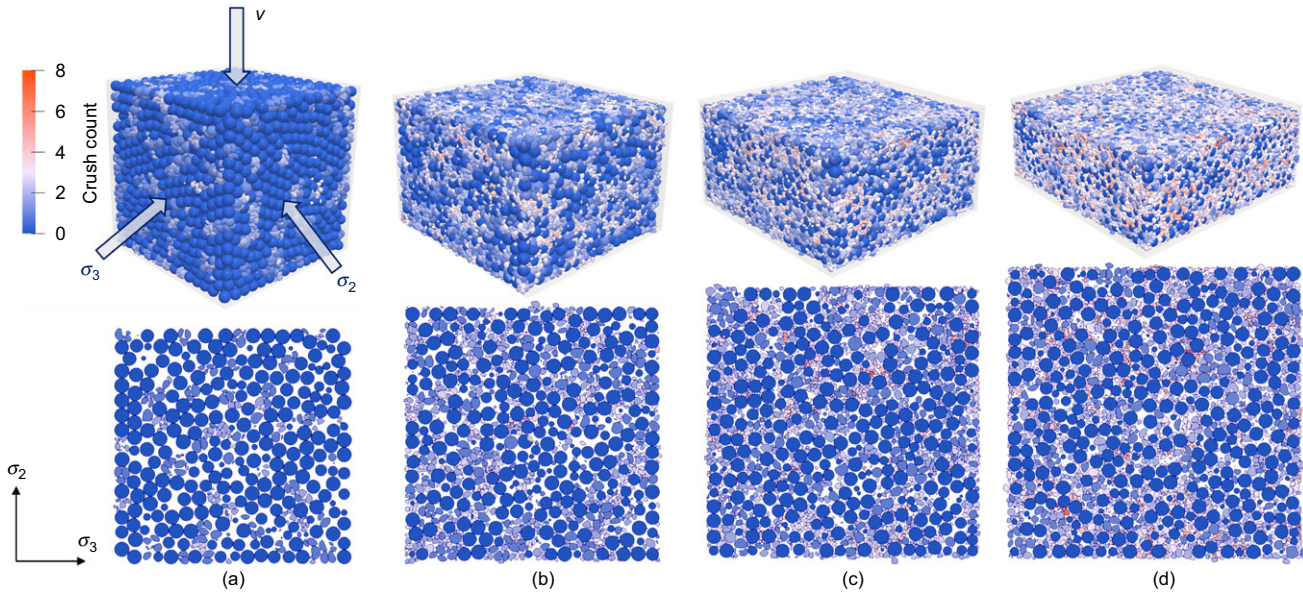


Fig. 2. Snapshots of the crushing process of a crushable sample under shearing with  $b = 0.0$  at different strain levels: (a) initial condition; (b) axial strain of 20%; (c) axial strain of 40%; (d) axial strain of 60%. The top row shows the entire 3D sample view and the bottom shows a cross-sectional view at half the height of the sample at a specific strain level. (The colour bar represents the number of breakages a particle has experienced during the shearing process.) A full-colour version of this figure can be found on the ICE Virtual Library ([www.icevirtuallibrary.com](http://www.icevirtuallibrary.com))

During the shearing process, the confining pressure along the  $x$ -direction is kept constant, while a servo control algorithm is developed to adjust the force in the  $y$ -direction to maintain a constant intermediate principal stress ratio defined by

$$b = \frac{\sigma_2 - \sigma_3}{\sigma_1 - \sigma_3} \quad (8)$$

where  $\sigma_1$ ,  $\sigma_2$  and  $\sigma_3$  are the major, intermediate and minor principal stresses, respectively. Subsequently,  $b = 0$  refers to a triaxial compression and  $b = 1$  refers to a triaxial extension. A series of true triaxial test simulations with varying constant  $b$  values ( $b = 0.0, 0.25, 0.50, 0.75, 1.0$ ) is carried out in this study. To consider the comminution limit of natural sand (Kendall, 1978), particles with an equivalent diameter smaller than 0.25 mm are assumed to be non-crushable. To dissipate the kinetic energy in the sample and ensure quasi-static conditions, a certain number of NSCD time steps (600 in the present study) are run after each breakage analysis; during that time the newly generated child particles move and rearrange to form a stable contact network. To quantitatively measure the force balance in the granular assembly, an unbalanced force ratio is introduced for both individual particles and the granular system. The former refers to the ratio of unbalanced force on a particle to average force magnitude on that particle, while the latter is the average unbalanced force ratio for all the particles in the system. Particles are excluded from breakage analysis until an unbalanced force ratio smaller than 0.02 is achieved for both the particle and the system. In the current simulations, the unbalanced force ratio of the system is mostly kept within 0.015.

Both densities of the particles and containers are magnified by 30 times to enhance the stability of the simulation. The time step is carefully chosen at  $1 \times 10^{-5}$  s to avoid the inertia effect brought by mass scaling. The inter-particle friction coefficient  $\mu$  is set to be 0.3 to avoid excessive rolling (Huang *et al.*, 2014b; Melanz, 2016). Other simulation parameters and material properties used in the following simulations are summarised in Table 1. Fig. 2 shows snapshots of a typical crushing sample at different shearing

Table 1. Parameters adopted in the simulation of a sand sample

	Parameters	Value
Material properties	Young's modulus: GPa	100
	Poisson's ratio	0.15
	Density: kg/m <sup>3</sup>	2650
	Initial void ratio	0.593–0.636
	Inter-particle friction coefficient	0.3
	Particle boundary friction coefficient	0.0
NSCD model	Restitution	0.0
	Shearing velocity: m/s	0.05
	Time step: s	$1 \times 10^{-5}$
	Confining pressure: MPa	1.5, 6, 12
PD model	Number of iterations per step	500
	Weibull modulus	3.1
	Loading rate: N/s	$1.6 \times 10^6$
	Size limit for crushing check: mm	0.25
	Force threshold for crushing check: N	20
	Base critical energy release rate: J/m <sup>2</sup>	15

stages. To assure the accuracy of the NSCD modelling, especially at the initial stage with limited number of particles, two benchmark triaxial shear simulations are performed on a granular sample consisting of 5000 spherical particles with face-centred-cubic (FCC) packing and rhombic packing. The peak strengths obtained are compared with theoretical solutions (Thornton, 1979) where a reasonable match is found, with a relative error of less than 1.4%. Parameters and results of the benchmark study are summarised in Table 2.

#### MACROSCOPIC BEHAVIOUR

In total, 15 true triaxial tests with different  $b$  values ( $b = 0.0, 0.25, 0.50, 0.75, 1.0$ ) under three levels of confining pressures ( $\sigma_3 = 1.5$  MPa, 6 MPa, 12 MPa) are simulated to examine the influence of the general stress path on the behaviour of crushable sand. To begin with, the correlation between overall material responses is explored, including

**Table 2. Parameters and results of benchmark study of triaxial shear of regularly packed specimens modelled with NSCD**

Packing	Face-centred-cubic packing	Rhombic packing
Inter-particle friction coefficient, $\mu$	0.3	0.3
Confining pressure, $\sigma_3$ : MPa	1.5	1.5
Theoretical peak strength equation, $\sigma_1/\sigma_3$	$2(1+\mu)/(1-\mu)$	$(4+2\sqrt{2\mu})/(1-\sqrt{2\mu})$
Theoretical strength value	3.714	8.421
Simulation results	3.764	8.426
Relative error: %	1.35	0.06

Results are compared with theoretical solutions.

strength and deformation, and the breakage of granular sand under different loading conditions.

### Strength and deformation

Two commonly used indicators in soil mechanics are employed to measure the shear strength of the simulated sand samples: the mobilised friction angle  $\phi_m = \sin^{-1}[(\sigma_1 - \sigma_3)/(\sigma_1 + \sigma_3)]$  and the stress ratio  $\eta = q/p'$ , where the mean effective stress  $p'$  and the deviator stress  $q$  are given by

$$p' = \frac{\sigma_1 + \sigma_2 + \sigma_3}{3} \quad (9)$$

$$q = \sqrt{\frac{(\sigma_1 - \sigma_2)^2 + (\sigma_2 - \sigma_3)^2 + (\sigma_1 - \sigma_3)^2}{2}} \quad (10)$$

where the principal stresses  $\sigma_1$ ,  $\sigma_2$  and  $\sigma_3$  are calculated from the reaction forces measured from the container boundaries. The stress tensor proposed by Christoffersen *et al.* (1981) is also used to compute stresses from the internal structure of the assembly, which will be analysed in later sections. It is noted that almost identical results are obtained with the two stress measures. Based on equations (9) and (10), the stress ratio is then calculated by  $\eta = q/p'$  in the following discussion.

The deformation of crushable sand specimens under shear is characterised by the axial strain  $\varepsilon_1$  and volumetric strain  $\varepsilon_v$ , defined as the integration of incremental strain given by

$$\varepsilon_1 = \int d\varepsilon_1 = \int_H^{H_0} \frac{dh}{h} = \ln \frac{H_0}{H} \quad (11)$$

$$\varepsilon_v = \int d\varepsilon_v = \int_V^{V_0} \frac{dv}{v} = \ln \frac{V_0}{V} \quad (12)$$

where  $H_0$ ,  $H$ ,  $V_0$  and  $V$  are the initial and current height and volume of the simulated sample, respectively. Positive volumetric strain indicates contraction.

Figure 3 shows the effects of  $b$  and confining pressure  $\sigma_3$  on the mobilised friction angle. For samples under the 1.5 MPa confining pressure, the mobilised friction angle is calculated using the peak strength; for samples under the confining pressures of 6 MPa and 12 MPa, where no apparent peak strength is identifiable owing to their contractive behaviour, the mobilised friction angle adopts an average value after 40% axial strain. Evidently, Fig. 3 indicates that the mobilised friction angle of crushable sand shows an initial increase with  $b$  and reaches a maximum value at around  $b = 0.5$ , before gradually dropping with  $b$ . In the two extreme cases,  $\phi_m$  in triaxial extension tests ( $b = 1.0$ ) is larger than that in triaxial compression tests ( $b = 0.0$ ), which is in good agreement with previous experiments (Xiao *et al.*, 2014).

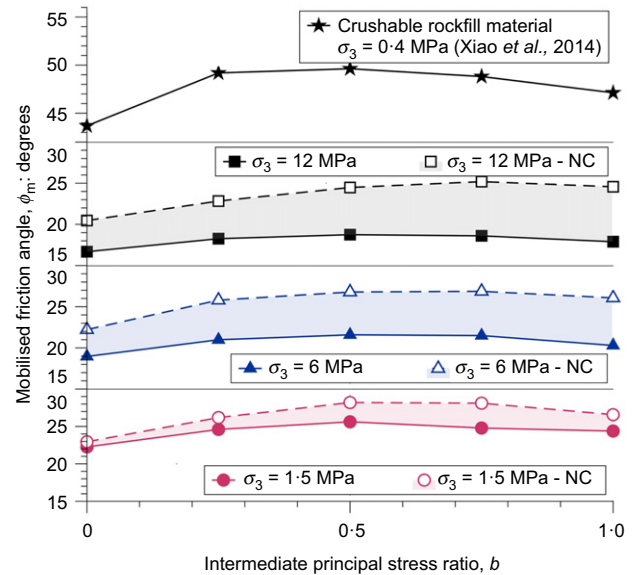


**Fig. 3. Variation of mobilised friction angle with  $b$ : comparison between experiment and the authors' simulation**

This implies that the conventional triaxial test ( $b = 0.0$ ) provides the most conservative strength, which is 10% and 25% lower than the strength from other stress paths. For comparison purposes, similar simulations are also performed on identical specimens with non-crushable grains and presented in Fig. 3 as marked by 'NC'.  $\phi_m$  for crushable sand appears to be more sensitive to the change of confining pressures than  $b$  in view of the appreciable reduction of  $\phi_m$  under higher confining pressures. The crushable specimens attain a maximum  $\phi_m$  at a slightly smaller  $b$  value (at around 0.5) as compared to their non-crushable counterparts (e.g. at around 0.75 for the case of  $\sigma_3 = 12$  MPa).

Figure 4 presents the evolution of stress ratio  $\eta = q/p'$  with axial strain. Compared with non-crushable cases, the crushable specimens under 12 MPa confining pressure exhibit a strain-hardening behaviour with a rapid increase of stress ratio at the initial shearing stage, followed by a slow increase or largely constant value after 30% axial strain. The specimens in the case of 1.5 MPa confining pressure undergo the least breakage events, helping them to attain a peak strength before softening, which resembles their non-crushable counterparts. They also show similar ultimate stress ratios (average stress ratio after 40% axial strain) to the non-crushable cases. It is noteworthy that the absolute values of mean and deviatoric stresses are different in the two cases. The present simulations show that particle breakage leads to an apparent reduction of peak stress ratio. Increasing the confining pressure may further suppress the ultimate stress ratio. The observation is consistent with past experimental and numerical studies (Wang & Yan, 2012; Yu, 2017c).

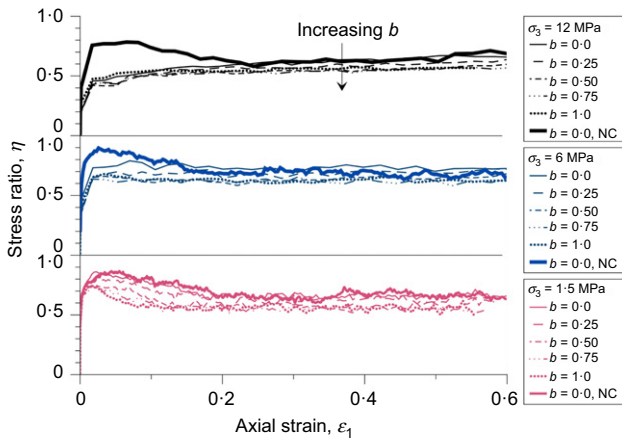
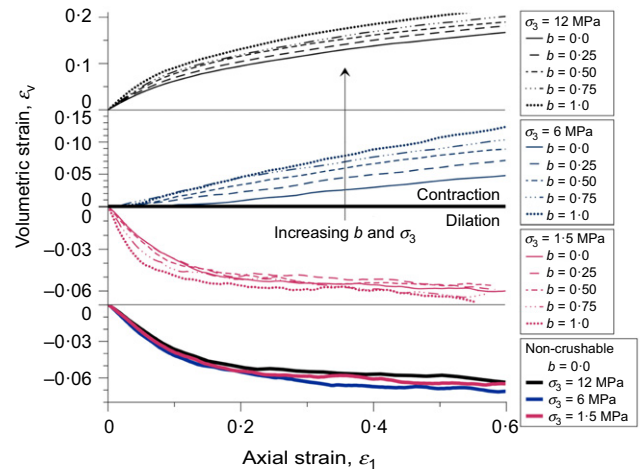


Fig. 4. Evolution of stress ratio ( $\eta = q/p'$ ) plotted against axial strain

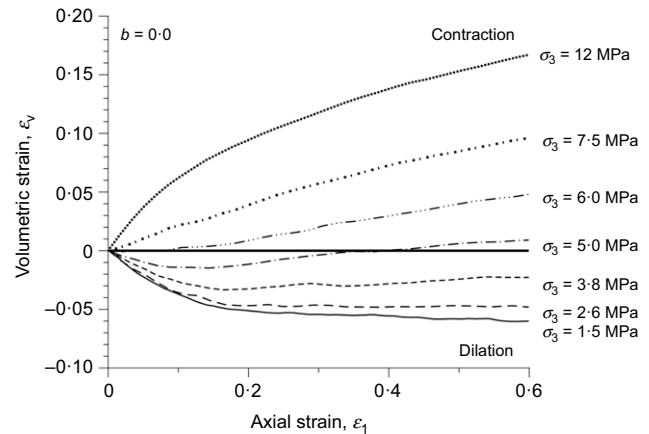
The volumetric behaviour of the crushable specimens is presented in Fig. 5 in comparison with the non-crushable cases. As shown in Fig. 5(a), non-crushable specimens and crushable ones under  $\sigma_3 = 1.5$  MPa exhibit dilative behaviour due to particle rearrangement. By contrast, cases with crushable particles show a clear transition from dilation to contraction under increasing confining pressures – for example, in the cases of  $\sigma_3 = 6$  MPa – and they become dominantly contractive at  $\sigma_3 = 12$  MPa. The degree of volumetric contraction also increases with  $b$  in the high-confinement cases. Fig. 5(b) further presents a comparison of more refined cases at  $b = 0.0$ , where the dilatancy transition from dilative to contractive behaviour can be best manifested in the case of  $\sigma_3 = 5$  MPa. Fig. 5(c) presents how the rate of dilation  $d\varepsilon_v/d\varepsilon_1$  (the ratio of incremental volumetric strain to incremental major principal strain) changes at different loading stages for the cases under  $\sigma_3 = 12$  MPa. The rate of dilation is positively correlated with  $b$  over a brief initial loading stage before reaching a peak at around 2% axial strain. The post-peak dropping rate of the dilation rate is also positively proportional to  $b$  until all cases converge to a mildly decreasing rate, which is largely independent of  $b$  after 30% axial strain. The high confinement of  $\sigma_3 = 12$  MPa causes intensive crushing, which generates a significant number of fine particles to fill void space, leading to the contractive behaviour of crushable sand. Such a mechanism of void filling due to evolving grain size will be discussed later in this paper. Under continued shearing, the specimens become more compacted, with more small particles joining the load-bearing structure, the crushing rate gradually decreases towards a stable level (this is further elaborated in the later section entitled ‘Particle crushing statistics’), leading to a constant non-zero dilatancy rate at large axial strain. The constant volumetric strain (or zero dilatancy rate) expected in a typical critical state condition is not observed for these cases of high confining pressure, and particle breakage is found to last throughout the shearing process. Similar behaviour was observed in previous ring shear tests on carbonate sand by Coop *et al.* (2004), showing that crushing and volumetric contraction continue to develop at strain levels as high as 1000.

Particle size and shape evolution

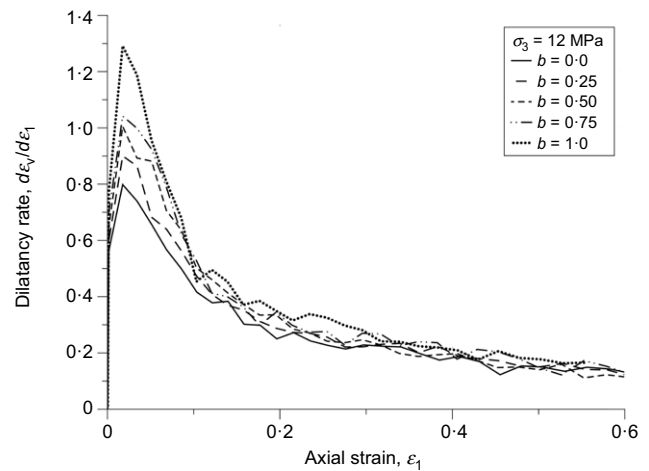
Figure 6 presents the evolution of PSD for some representative cases ( $\sigma_3 = 12$  MPa). Fig. 6(a) shows the continuous evolution of PSD for the case  $b = 0.0$ . Notably, continuous shearing pushes the PSD curve moving upwards because of progressive breakage of large original particles. It



(a)



(b)



(c)

Fig. 5. Evolution of (a) volumetric strain with  $b$ ; (b) volumetric strain with varying confining pressures for  $b = 0.0$ ; (c) dilatancy rate plotted against axial strain

is found that over half of the original particles survive the shearing at large strains. A kink in the evolution curves at size  $d = 1.0$  mm is also presented, which is likely to be a result of the particular size and shape of particles adopted in the simulation. A similar feature can also be observed in experiments on uniformly distributed sand samples, including the ring shear tests (Luzzani & Coop, 2002; Wei *et al.*, 2021), triaxial compression tests (Karatzas *et al.*, 2018) and impact load tests (Lin *et al.*, 2020). This feature is more apparent when a mono-dispersed packing with identical

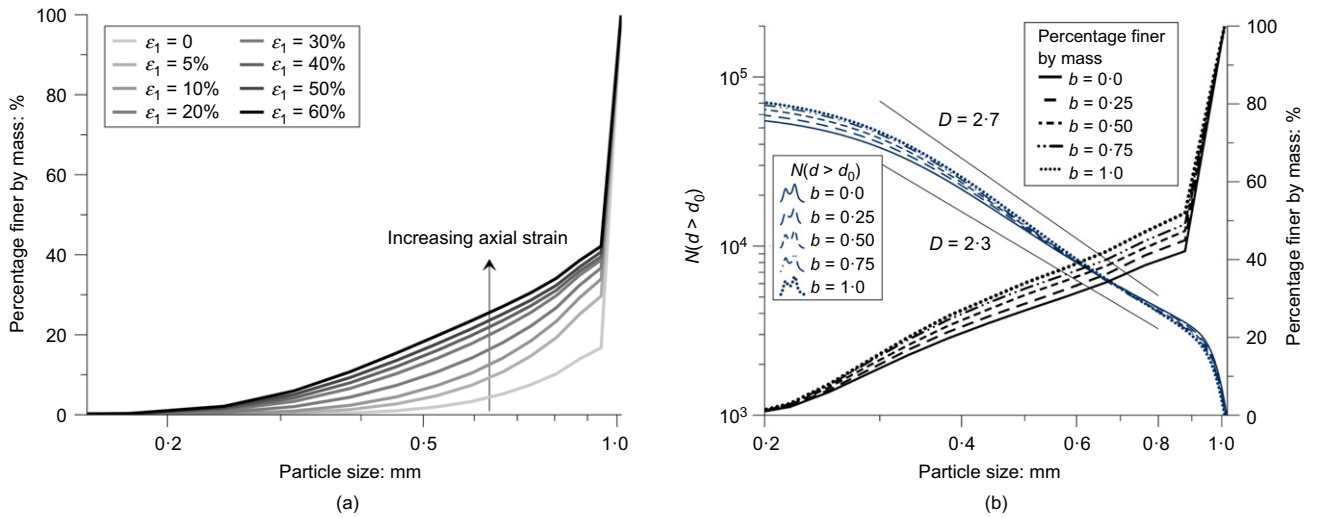


Fig. 6. (a) Evolution of particle size distribution for the specimen sheared at  $b=0.0$ ,  $\sigma_3=12$  MPa and (b) ultimate particle size distributions for all specimens sheared under  $\sigma_3=12$  MPa at 60% axial strain. (Herein the particle size is quantified by its principal axis but not the diameter of an equal-volume sphere to offer better comparability with common experimental works)

particle shape (i.e. spheres) is used, as in the present study. With the progress of particle crushing, the surviving large particles are surrounded by an increasing number of small particles (see Fig. 2(d)), resembling the typical ‘cushioning effect’ observed in laboratory tests (Tsoungui *et al.*, 1999; Zhong *et al.*, 2018). The structure better accommodates force transmission around the large particles to mitigate further breakage before an ultimate steady-state size distribution is reached.

Figure 6(b) shows the ultimate PSD of all five cases of  $b$  at the same confining pressure of 12 MPa at 60% axial strain, presented in both linear and logarithmic vertical axes. The results indicate the increase in intermediate principal stress ratio  $b$  may cause the specimen to develop a finer gradation evolving towards an ultimate fractal distribution. The fractal dimension is only identifiable by plotting particle size with the cumulative number of particles larger than the size,  $N(d > d_0)$ , in a log–log space and the slope of the curves is measured to be the fractal dimension,  $D$ . Evidently, the fractal dimension is not a constant but varies with  $b$ . An increase in  $b$  leads to a higher fractal dimension, indicating a denser packing with better space-filling capacity. The obtained fractal dimension ranges from 2.3 ( $b=0.0$ ) to 2.7 ( $b=1.0$ ), which is comparable with observations from 1D compression tests (Zhong *et al.*, 2018). The study by De Bono & McDowell (2018) suggests that, when a critical state is reached, a corresponding unique PSD curve is attainable regardless of the stress path. As will be discussed in a later section, there are complications in defining critical state in crushable sand, and whether a unique PSD has to be coinciding with the critical state for crushable sand remains an open question to be explored.

To offer a deeper insight into the crushing-induced change in gradation, the classical Hardin’s breakage index (BI) (Hardin, 1985) can be examined for all the simulated cases. As shown in Fig. 7, BI undergoes a faster increase at lower strain levels (e.g. under 10% of axial strain) and begins to maintain a constant increasing rate with axial strain. It continues to rise even at the end of shearing – that is, at an axial strain of 60% – indicating that particles do not cease to crush at such a high strain level.

Particle shape changes during the crushing process and plays a pivotal role in determining the internal structure and mechanical properties of granular sand. The multi-scale computational model employed in this study offers the

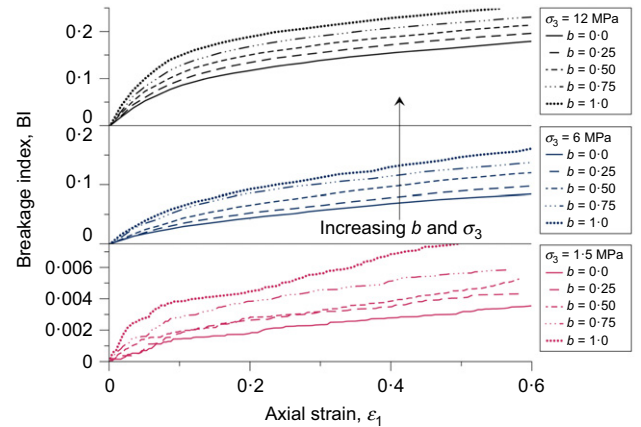


Fig. 7. Evolution of Hardin’s breakage index BI with axial strain

capability to realistically simulate and examine the changing particle shape during crushing. Sphericity has been regarded as a representative shape factor to characterise particle shape and is employed here to gauge the shape evolution. Other shape factors, such as aspect ratio, elongation and flatness, have all been found to play a similar role (Zhu & Zhao, 2019a, 2021b). Sphericity measures the deviation of particle shape from a perfect sphere, as defined by

$$\Psi = \frac{\sqrt[3]{36\pi V_p^2}}{A_p} \quad (13)$$

where  $V_p$  and  $A_p$  are the volume and surface area of the measured particle, respectively. A higher sphericity refers to a particle shape closer to a sphere.

The evolution of the cumulative distribution of sphericity excluding the original spherical particles is plotted in Fig. 8(a) for a characteristic case of  $\sigma_3=12$  MPa and  $b=0.0$ , which experiences significant particle crushing. Clearly, the crushing of particles drives the evolution of the particle shape distribution to shift leftwards. For initially spherical particles, crushing leads to more elongated and irregular shapes, as represented by the reducing sphericity. Meanwhile, irregular particles tend to evolve towards higher sphericity due to the chipping effect. When sufficient

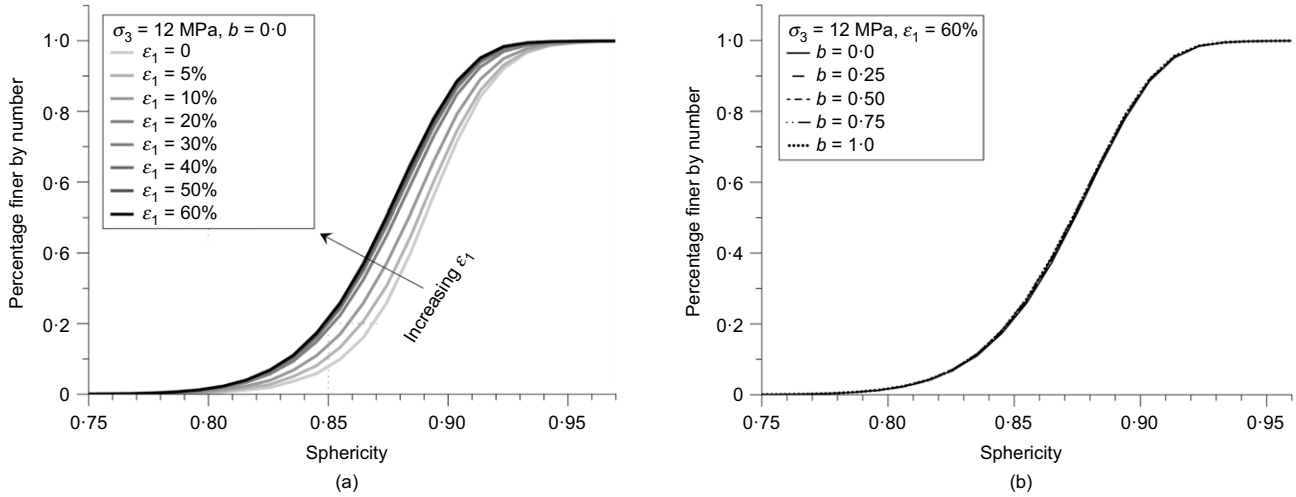


Fig. 8. (a) Evolution of cumulative distribution of sphericity for sample with  $b = 0.0$ ,  $\sigma_3 = 12$  MPa and (b) converged sphericity for specimens under  $\sigma_3 = 12$  MPa at 60% axial strain at different  $b$  values

crushing events occur at large shear strains, the differences among irregular and spherical shapes tend to reduce, and the shape distribution profile begins to converge to a stable state. For the same specimen subjected to different  $b$  loading paths, the ultimate cumulative distribution curves of sphericity at 60% axial strain are plotted in Fig. 8(b). Interestingly, a unique distribution profile independent of loading paths is identifiable. Confirmed by some early reports in experiments (Domokos *et al.*, 2015), the observation supports the idea that the fragment shape distribution is predominantly decided by the intrinsic material properties, especially its microstructures, rather than the loading conditions that the material may undergo.

Particle crushing statistics

The statistics of crushed particles at each strain increment are further examined quantitatively. The cases with a confining pressure of 12 MPa and different  $b$  values are chosen again for analysis since they involve most particle crushing events. The number of particle crushing events recorded at an interval of 2% strain increment, termed the crushing rate, is plotted against axial strain in Fig. 9. A peak crushing rate is observed in all cases, and it occurs earlier with a larger  $b$  value. The cases with large  $b$  also indicate a faster growth of pre-peak crushing rate and consequently more particle crushing events. This may be attributed to the higher mean stresses or confinements corresponding to the larger  $b$  value, which tend to cause more volumetric contraction and create a condition favouring the occurrence of crushing. The crushing rate gradually slows down during the post-peak stage, typically starting from around 10% of axial strain. The pre-peak rapid development of crushing events leads to the growing number of fine particles which fill the voids to support the large particles, reducing the crushing probability of the latter. At an axial strain of 60%, the crushing rate in all cases converges asymptotically to be largely independent of  $b$ . The convergence reveals a unique balance of increasing crushed particle numbers and reduced average contact forces in a granular assembly that is largely independent of the loading path. More specifically, cases with larger  $b$  exhibit more pre-peak crushing events and consequently higher coordination number and quicker redistribution of external loads during the post-peak stage to reduce the average contact forces, leading to faster convergence to the asymptotic state at large shear strain.

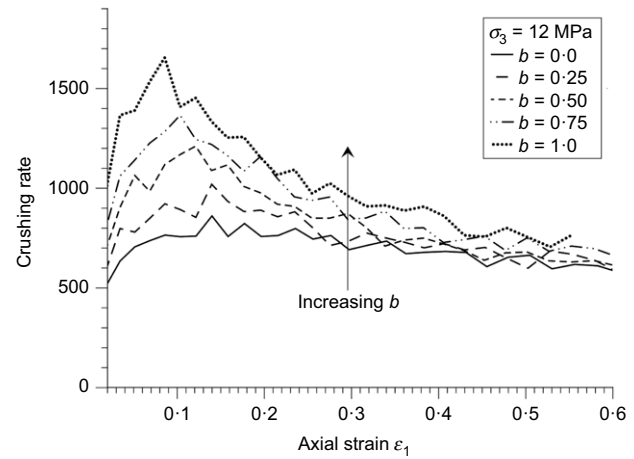


Fig. 9. Change of crushing rate (defined by the number of crushing events per 2% strain increment) with axial strain

Figure 10(a) presents the evolution of crushing probability, which is defined as the number of broken particles normalised by the number of existing particles within each size group, for the simulation case of  $b = 0.0$ ,  $\sigma_3 = 12$  MPa. The shaded areas represent the crushing probability of each size group, while the lines correspond to the cumulative crushing probability summed over each group. As shearing initiates, the crushing probability for large particles decreases rapidly and becomes the lowest as a result of the ‘cushioning effect’, as illustrated in Fig. 11. The surrounding child particles formed after substantial crushing provide support and distribute contact forces targeted for large particles so that they barely meet the crushing criterion despite their lower strength compared to the smaller particles (as per equation (4)). Meanwhile, small particles ( $d < 0.5$  mm) possess higher strength than medium-sized particles ( $d = 0.5-0.9$  mm) according to Weibull theory. Consequently, the medium-sized child particles become the major source of breakage after 20% axial strain. The particle crushing probability and intensity, as presented in Figs 9 and 10, are affected by loading conditions at small strains, but such effect is mitigated after an endured fragmentation process.

A breakage ratio is further defined as the ratio of the number of newly generated child particles to the number of broken particles at each strain increment. It is used to

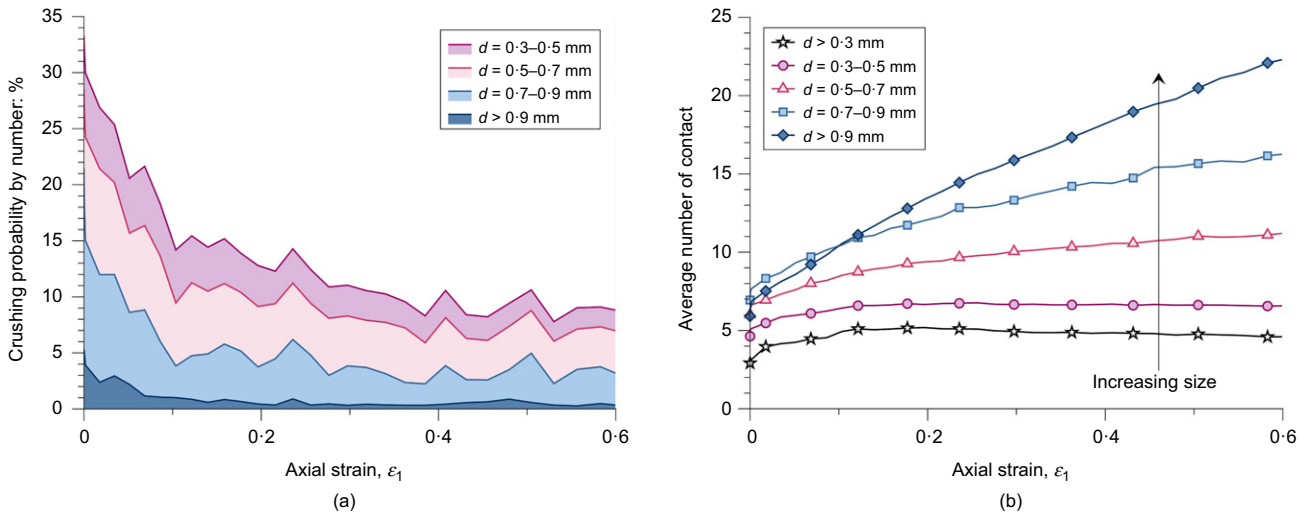


Fig. 10. (a) Crushing probability and (b) average contact number of particles in different size groups plotted against axial strain. A full-colour version of this figure can be found on the ICE Virtual Library ([www.icevirtuallibrary.com](http://www.icevirtuallibrary.com))

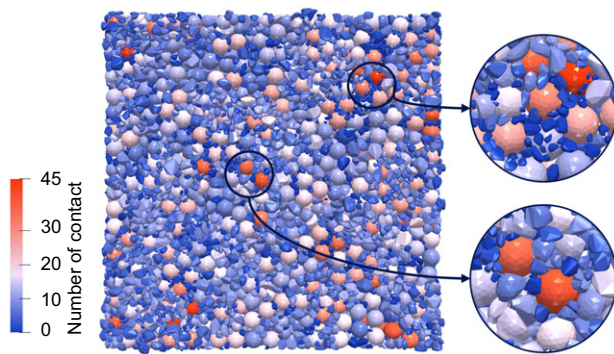


Fig. 11. Illustration of 'cushioning effect' in sample with  $b = 0.0$ ,  $\sigma_3 = 12$  MPa at 60% axial strain. A full-colour version of this figure can be found on the ICE Virtual Library ([www.icevirtuallibrary.com](http://www.icevirtuallibrary.com))

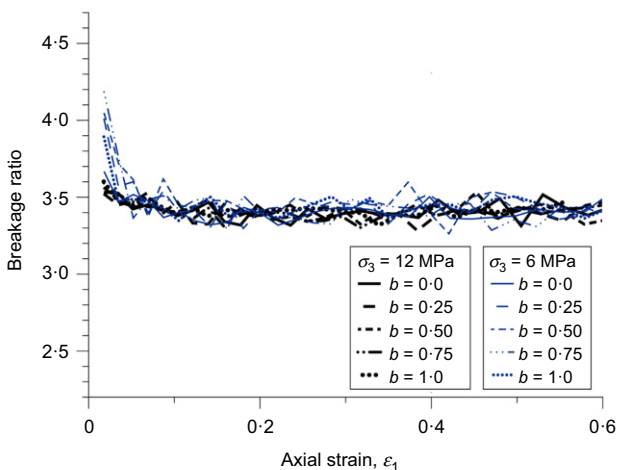


Fig. 12. Evolution of breakage ratio with axial strain

quantify the crushing patterns and predict the evolution of particle size distribution. Fig. 12 shows the variation of the breakage ratio with the axial strain, from which a unique breakage ratio of about 3.4 is identified for all cases of confining pressures of 6 MPa and 12 MPa, indicating that a particle tends to break into 3–4 pieces regardless of the loading conditions. Note that the conclusion is herein

reached with the assumption of a linear elastic isotropic material that has undergone brittle failure for each grain, and the counting of particles only considers the major broken pieces by neglecting fine fragments (i.e.  $< 3\%$  volume of the parent particle) obtained in the PD simulation. The above observation appears to imply that the particle crushing characteristics, in terms of the number of major fragments, is more of a material property and less associated with loading conditions.

#### MICROSCOPIC RESPONSES

While the general stress conditions affect various facets of the macroscopic behaviour of crushable granular sand in a profound and intricate manner, the continuum-scale responses have their microstructural origins. The multi-scale computational approach enables further examination of these microscopic mechanisms that possibly account for the macroscopic observations and hence furnishes a better understanding of crushable sand.

#### Coordination number

Coordination number has been frequently used in micro-mechanics of granular media to measure the number of contacts a particle possesses. Its average over a granular assembly helps to characterise the internal contact network of the particles in relation to their load-bearing capacity. In this study, the evolution of the mechanical coordination number of particles with the shear strain is examined. The mechanical coordination number is defined by

$$Z_m = \frac{2N_c}{N_p} \quad (14)$$

where  $N_c$  represents the total number of contacts and  $N_p$  represents the total number of particles excluding rattlers with zero or one contact. The evolution of  $Z_m$  for all cases under  $\sigma_3 = 12$  MPa is plotted in Fig. 13.  $Z_m$  is found to undergo a rapid increase at the initial shearing stage due to the occurrence of substantial breakage events that produce an increasing number of child particles. It reaches a steady value between 7.5 and 8.5, or slightly decreases for all cases after 20% of axial strain. The ultimate value of  $Z_m$  is closely related to particle breakage and loading conditions. Crushable specimens show a much higher  $Z_m$  than a value

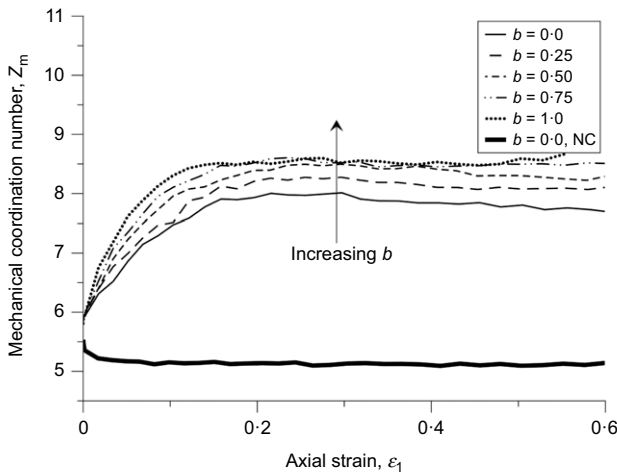


Fig. 13. Evolution of mechanical coordination number  $Z_m$  with axial strain under  $\sigma_3 = 12$  MPa. NC, non-crushable

around 5 for the non-crushable comparison case shown in Fig. 13. A higher  $Z_m$  is reached with a higher  $b$  value due to more significant particle breakages caused by stronger confinements.

The well-known ‘cushioning effect’ is indeed directly reflected by the increasing coordination number of particles during the crushing process. Fig. 13 appears to imply that the cushioning effect develops mainly in the first 15% axial strain or so before maturing. This proves to be not true after examining the average coordination number for particles in different size groups in Fig. 10(b). Clearly, the average coordination number for large particles ( $d > 0.5$  mm) shows a continued increasing trend even at large axial strains and the increasing rate is positively correlated with particle size. The ‘cushioning effect’ therefore continues to develop to offer improved protection for those large particles if particle crushing continues to occur. For smaller particles ( $d < 0.5$  mm), however, their coordination number only exhibits a slight increase shortly after the commencement of shearing and stays nearly stable or even drops throughout the rest of the simulation. The largely steady or slightly decreased coordination number observed in Fig. 13 is due to the unweighted average of contact numbers calculated by equation (14) when the small, crushed particles with fewer contacts are massive in number and play a more prominent role in the mechanical coordination number evolution. For conciseness, not all of the results for the different combinations of  $b$  and confining stresses are shown. Nonetheless, the results presented indicate that a larger  $b$  condition is associated with stronger crushing, a more compacted packing, a higher and stable mechanical coordination number, and a stronger ‘cushioning effect’ for large particles.

#### Particle level contact force network

The mean contact force  $f_n$  has been widely used to assess the stress condition inside a granular assembly. Fig. 14 shows the evolution of the mean contact force in simulations under  $\sigma_3 = 12$  MPa with different  $b$  values. In all cases, the mean contact force shows a rapid decrease over the initial stage of shearing due to significant particle crushing, before slowing down after 20% of axial strain and gradually converging to a steady state. Cases with larger  $b$  show a steeper initial drop in  $f_n$  and a slightly lower steady-state value of  $f_n$ . This is consistent with the observation in Fig. 9, where cases with larger  $b$  were found to have a higher crushing rate, indicating more crushed particles in the assembly to participate in the

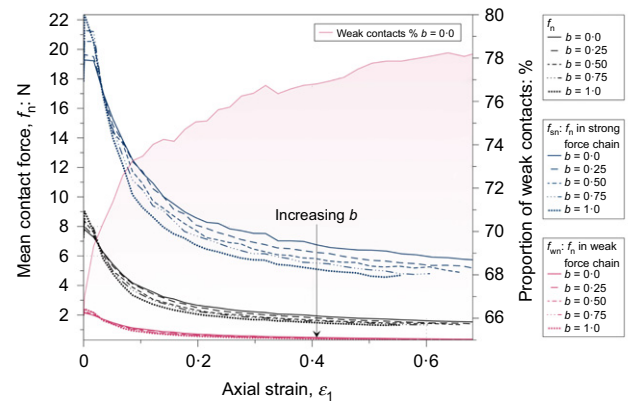
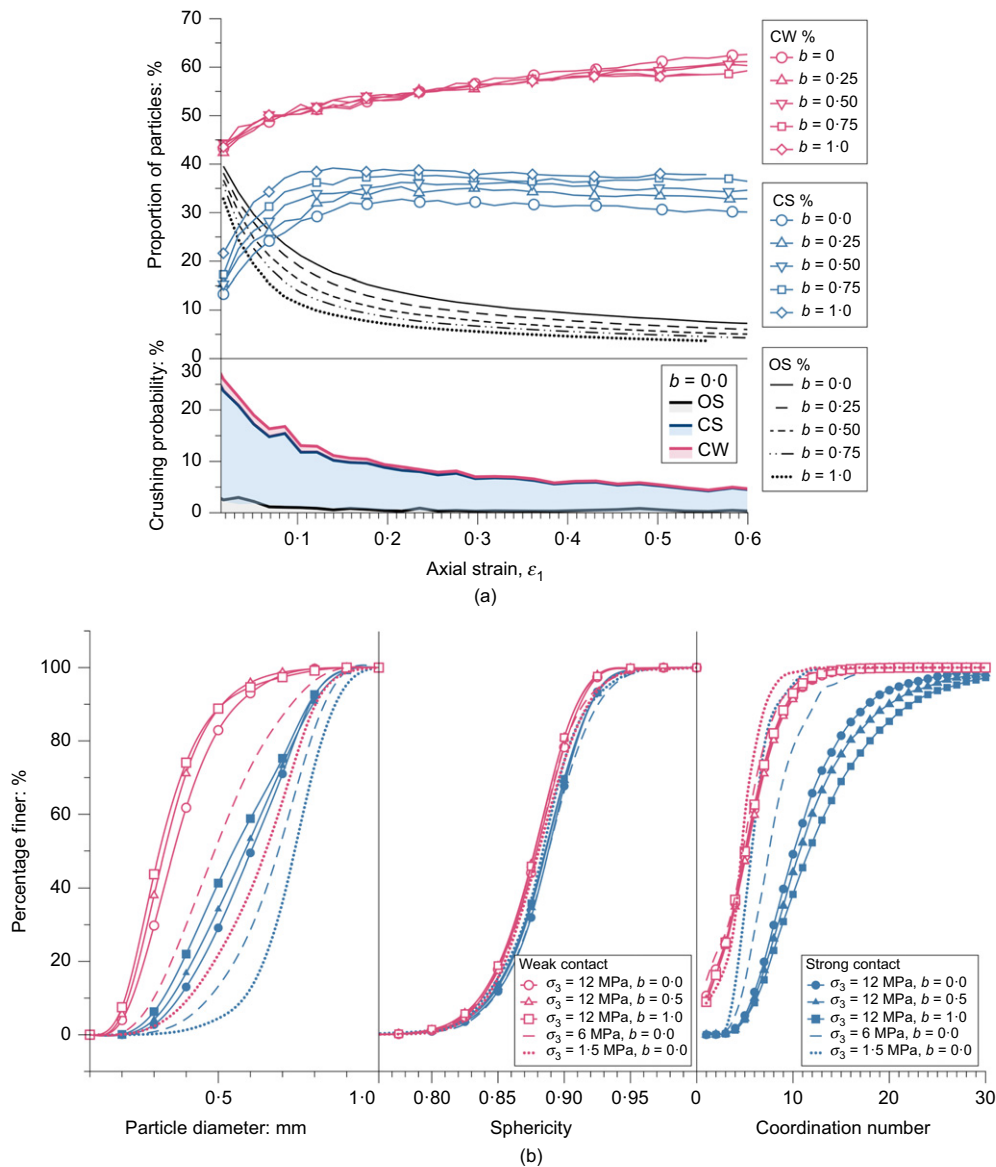


Fig. 14. Evolution of contact forces and weak contact proportion for specimens under  $\sigma_3 = 12$  MPa. A full-colour version of this figure can be found on the ICE Virtual Library ([www.icevirtuallibrary.com](http://www.icevirtuallibrary.com))

force transmission and lower the average contact force on particles.

It is well recognised that the force transmission in a granular assembly features a dichotomy of strong and weak force networks, bounded by the mean contact force, each playing a unique role in sharing the load exerted on the material (Radjai *et al.*, 1998; Guo & Zhao, 2013). The strong force chains, referring to those carrying larger than average normal contact force, are the backbone of an assembly sustaining the majority of deviatoric stresses, whereas the weak force chains, with contact forces below the average, constitute the majority of the contact force network and provide lateral support for the strong force chains. Fig. 14 presents the proportion of strong and weak contacts normalised by total contacts extracted from the current simulations. The proportion of weak force chains depicts a steady increase to reach over 78% of total contacts at 60% axial strain, accompanied by a steady decrease of average contact force in both the strong and weak force networks. Magnitude wise, the average contact force in a strong force network can reach 10 times higher than that in the weak force network. The average contact force in strong force chains is more significantly influenced by the intermediate principal stress, showing a relatively wide band over the different  $b$  ranges. The weak force chains exhibit a rather concentrated stable average contact force which can be largely regarded as independent of  $b$ . The high consistency of variation of macroscopic strength and peak friction angle with strong force chains under different intermediate principal stress ratios is indeed attributed to the dominance of strong force chains in the force transmission of the entire contact force network.

A further inspection on the type of particles participating in the strong and weak force chains is presented in Fig. 15 for cases under  $\sigma_3 = 12$  MPa. For particles that survived the shearing process, the numbers of original particles in the strong force chain  $N_{OS}$ , original particles in the weak force chain  $N_{OW}$ , child particles (formed due to breakage) in the strong force chain  $N_{CS}$ , and child particles in the weak force chain  $N_{CW}$  normalised by the total number of particles in contact  $N_T$  are plotted as a function of axial strain in Fig. 15(a). It is found that more than 90% of the original particles participate in the strong force network during the crushing, leading to negligibly small  $N_{OW}/N_T$ , which is omitted in the discussion for the sake of simplicity. Over half of the child particles are found to participate in the weak force chains and their proportion is insensitive to the intermediate principal stresses. The majority of breakage events occur to the child particles that join the strong force chain, although their proportion in the overall assembly is less than 40%.



**Fig. 15. (a) Proportion of existing original and child particles. (b) Particle size, shape and coordination number distribution in strong and weak contact networks under  $\sigma_3 = 12$  MPa. A full-colour version of this figure can be found on the ICE Virtual Library ([www.icevirtuallibrary.com](http://www.icevirtuallibrary.com))**

Figure 15(b) presents the distribution of size, shape and coordination number of particles in strong and weak force chains. Particles joining strong force chains are distinguished by larger size, higher coordination number and rounded shape compared with their counterparts in weak force chains. The intermediate principal stress has a more appreciable influence on the particle size and coordination number distribution in strong force chains as more child particles participate in strong force chains with increasing  $b$ . The particle shape in both strong and weak force chains shows less dependency on the stress conditions. Although particle crushability is governed by the coupled effect of particle size, shape, coordination number and contact force, the influence of contact force appears to prevail over the other factors in the shearing process. As shown in Fig. 15(a), the breakage potential of particles in the strong force chain is obviously higher, even though their higher coordination number and more regular shape help to spread contact forces to counterfeit the chance of breakage. For those smaller particles broken in weak force chains, the stress concentration brought by lower contact number and irregular shape outweighs their increasing strength by decreasing particle size.

### Anisotropy

Fabric anisotropy can help to elucidate the microstructure of the contact network in crushable samples under general stress conditions. Herein a three-dimensional (3D) histogram of the distribution of contact forces and contact normal is employed as a full-scale representation of the contact network in an assembly. The length and colour of each bar in the figure represent the average magnitude of the normal contact forces  $\bar{f}_i$  normalised by  $f_n$  orientated along the corresponding direction. A spherical shaped 3D histogram corresponds to an isotropic distribution of normal contact force and more elongated ones indicate anisotropy in the granular assembly. Fig. 16 illustrates the evolution of the strong and weak contact force network for a triaxial compression sample under 12 MPa confining pressure. Evidently, the weak contact force network becomes more isotropic during the loading process, while the strong contact force exhibits strong shear-induced anisotropy, as reflected by the extended histogram in the shearing direction. The anisotropy for strong contact force reaches a peak at 20–30% axial loading, which synchronises with the trend of observed breakage events as shown in Fig. 9. The influence

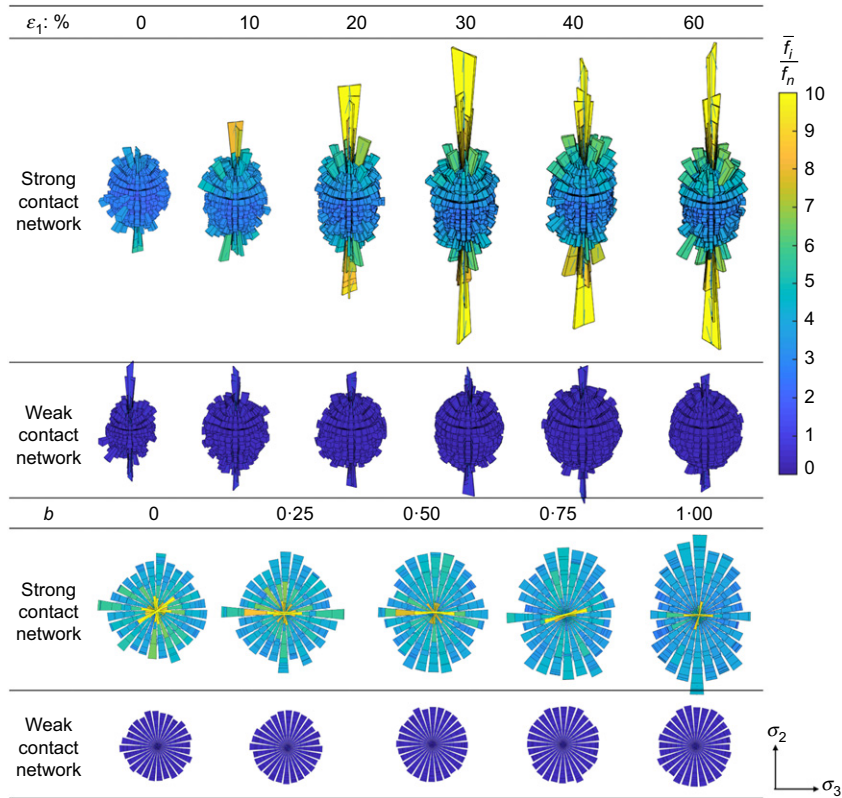


Fig. 16. Evolution of strong and weak contact network for the simulation cases

of intermediate principal stress on the anisotropy of normal contact force is also depicted in Fig. 16. The strong contact force histogram is stretched towards the  $\sigma_2$  direction as  $b$  increases, while the influence of  $b$  on the weak contact network is not obvious. Evidently, the shear-induced anisotropy is closely related to the intermediate principal stress,  $\sigma_2$ .

Several methods (Rothenburg & Bathurst, 1989; Oda & Iwashita, 2020) have been proposed to quantify the anisotropy of the contact network and shear strength in granular packings. The stress tensor  $\sigma_{ij}$  and fabric tensor  $\Phi_{ij}$  are frequently used to examine the contribution of force and fabric anisotropies to the overall shear strength, and their discrete-based expressions are given by

$$\sigma_{ij} = \frac{1}{V} \sum_{c \in N_c} f_i^c d_j^c \quad (15)$$

$$\Phi_{ij} = \frac{1}{N_c} \sum_{c \in N_c} n_i n_j \quad (16)$$

where  $V$  and  $N_c$ , respectively, refer to the volume and the total number of contacts of the assembly;  $f_i^c$  is the contact force at contact  $c$  in direction  $i$ ;  $d_j^c$  is the branch vector connecting the centres of two contacting particles; and  $n$  is the unit vector along the direction of contact normal. Based on equations (15) and (16), the mean effective stress  $p'$ , deviator stress  $q$  and the degree of contact normal anisotropy  $A_c$  can be further derived according to

$$p' = \frac{1}{3} \sigma_{ij}, \quad q = \sqrt{\frac{3}{2} \sigma'_{ij} \sigma'_{ij}} \quad (17)$$

$$a_{ij}^c = \frac{15}{2} \Phi_{ij}, \quad A_c = \sqrt{\frac{3}{2} a_{ij}^c a_{ij}^c} \quad (18)$$

where  $\sigma'_{ij}$  and  $\Phi'_{ij}$  are the deviatoric part of the stress tensor and fabric tensor, respectively. Note that  $p'$  and  $q$  defined in equation (17) are calculated from a micromechanics-based stress tensor in equation (15) based on inter-particle contact forces. They have been verified to be identical to those defined in equations (8) and (9) measured from the boundaries.

The discrete definition of a stress tensor and a fabric tensor allows a unique decomposition of strength and anisotropy into the following four parts

$$\sigma = \sigma_{os} + \sigma_{ow} + \sigma_{cs} + \sigma_{cw} \quad (19)$$

where the four groups of contacts marked as subscripts are defined as follows: (a) 'os' and (b) 'ow' refer to contact between two original particles (unbroken particles from the original packing) measured as strong and weak contact force, respectively; (c) 'cs' and (d) 'cw' refer to a contact involving one or both child particles in strong and weak force chains, respectively. Their contribution to the overall shear strength and peak friction angle can be identified through the decomposition of the stress tensor, and the corresponding  $\sigma_{os}$ ,  $\sigma_{ow}$ ,  $\sigma_{cs}$  and  $\sigma_{cw}$  are derived from equation (15) with restricted summation based on subgroups of contacts.

The stress ratio  $q_{os}/p'$ ,  $q_{ow}/p'$ ,  $q_{cs}/p'$  and  $q_{cw}/p'$  and the corresponding major principal stress  $\sigma_1$  for the different groups at ultimate state are shown in Fig. 17. The strength provided by the strong force chains is the dominant portion of the shear strength during the shearing process. Changes of stress ratio and mobilised friction angle with  $b$  are underpinned by the competition between the original and the child particles in the strong contact network. The decrease of  $q_{os}/p'$  marked by the darkest (blue) area is a result of the reduced number of surviving original particles under a higher intermediate principal stress ratio. New particles generated by breakage of original particles in turn contribute to the gradual increase of  $q_{cw}/p'$ , collectively leading to an

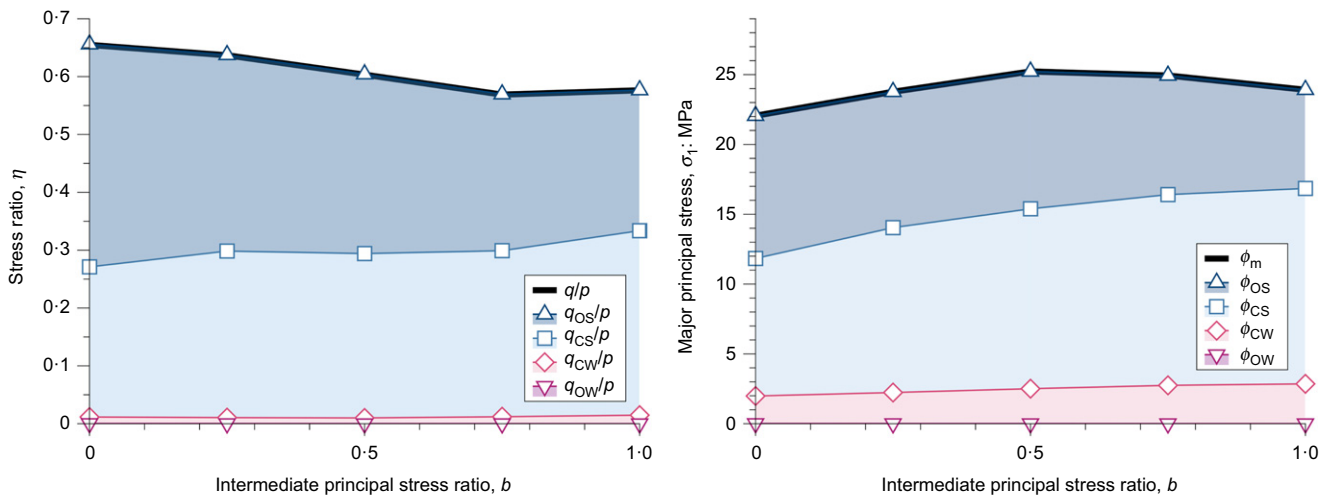


Fig. 17. Shear strength as a function of  $b$  under  $\sigma_3 = 12$  MPa for (a) stress ratio,  $\eta$ ; (b) major principal stress,  $\sigma_1$

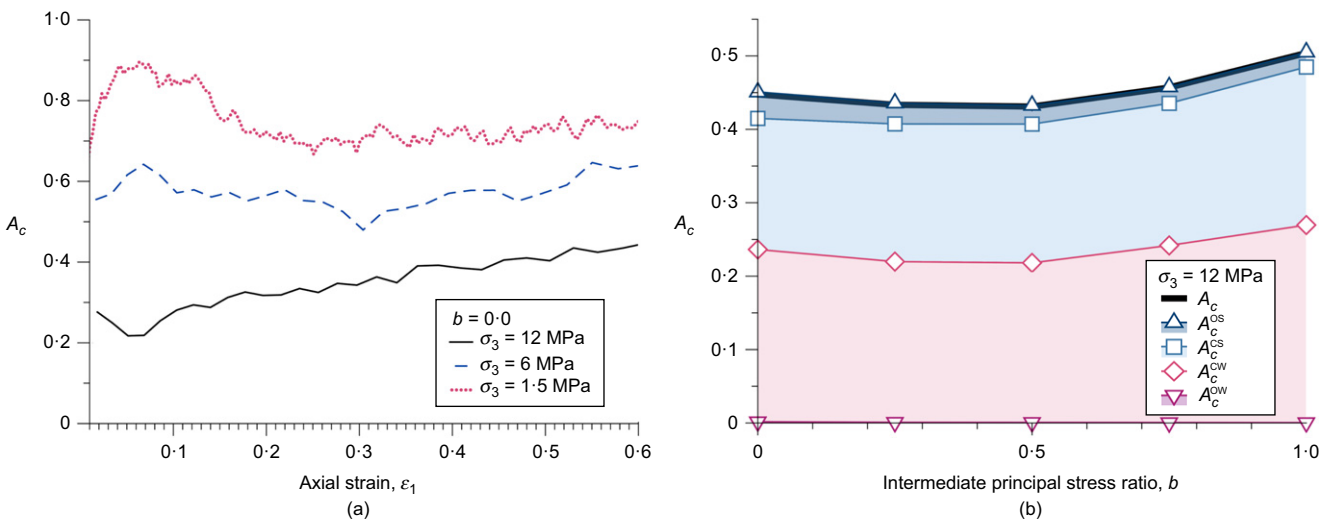


Fig. 18. (a) Evolution of contact normal anisotropy  $A_c$  with axial strain under various confining pressures at  $b = 0.0$ . (b) Change of  $A_c$  at ultimate states with  $b$  at  $\sigma_3 = 12$  MPa

overall suppressed stress ratio with increasing  $b$ . The mobilised friction angle  $\phi_m$  is influenced by  $b$  and breakage in a similar way. For simulations under a fixed confining pressure  $\sigma_3$ ,  $\phi_m$  is indeed controlled by the major principal stress  $\sigma_1$ . The increase of  $\sigma_1$  contributed by child particles in the strong contact chains is compensated by the decreased contribution owing to fewer original particles, which gives rise to the peak of mobilised friction angle at  $b = 0.5$ .

In Fig. 18(a) a further plot is provided of the evolution of contact normal anisotropy  $A_c$  of a granular assembly with axial strain for triaxial compression test samples under various confining pressures. Under such conditions,  $A_c$  strongly correlates with the stress ratio. A continuous growth of contact normal anisotropy  $A_c$  during shearing is observed wherein the increasing confining pressure has a reverse effect on the anisotropy due to the increasing polydispersity induced by continuous particle breakage, which correlates well with the changes of stress ratio.

The decomposition of the fabric tensor is also conducted based on a similar approach as stress ratio and the corresponding components  $A_c^{OS}$ ,  $A_c^{OW}$ ,  $A_c^{CS}$  and  $A_c^{CW}$  against  $b$  at ultimate state are plotted in Fig. 18(b). Notably, child particles involved in both strong and weak force chains develop a much higher contact normal anisotropy compared

with the original particles. With the increase of  $b$ ,  $A_c$  from child particles in the strong force chains increases monotonically, which is consistent with the extended shape of 3D histograms in Fig. 16. The contribution of the weak contact network to the contact normal anisotropy is also remarkable due to the overwhelming number ( $> 80\%$ ) of weak contacts. Fewer breakage events occur in specimens with  $b < 0.5$ , resulting in a coarser gradation with relatively higher anisotropy. Meanwhile, contacts tend to cluster in the  $\sigma_2$  direction with the increase of  $b$ , leading to increased contact normal anisotropy accordingly. As a result,  $A_c^{CW}$  slightly declines with  $b$  until a minimal value is approached at  $b = 0.5$ , then reverses before reaching its peak at the triaxial extension condition ( $b = 1.0$ ). The above analyses based on the decomposition of stress tensor and fabric tensor help to clarify the origin of shear strength and anisotropy in crushable granular materials and offer a reasonable explanation for the reduction of mobilised friction angle when the intermediate principal stress ratio  $b$  exceeds 0.5.

## DISCUSSION

The behaviour of crushable granular media is intriguingly complicated, as presented in the preceding sections. A brief

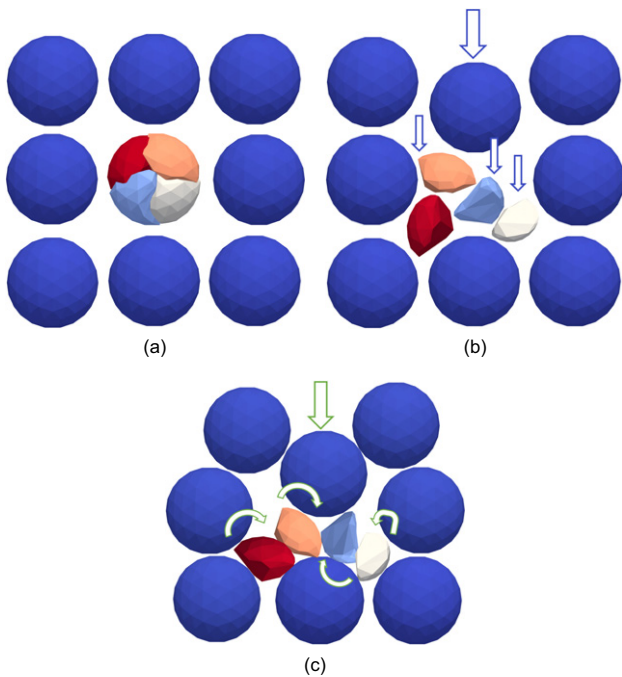


**Fig. 19. Illustration of two competing mechanisms on the deformation behaviour of crushable sand: (a) initiation of particle breakage; (b) child particles filling surrounding pores; (c) shape-enhanced resistance to particle movement and structural interlocking by the child particles**

discussion is further given here to explore the fundamental physics and mechanisms that may control the deformation and strength of crushable granular media under different external conditions and their connection with classic soil mechanics concepts, including critical state and dilatancy. To lead the discussion, the authors propose two competing mechanisms that account for the shear deformation in crushable granular sand, as illustrated in Fig. 19. The first refers to a void-filling mechanism when crushing causes the generation of smaller child particles to fill the pore space among bigger particles (Fig. 19(b)). This mechanism tends to lead to contractive behaviour for granular material. The other refers to an enhanced resistance and interlocking mechanism on grain motion and rearrangements due to irregular shapes of grains (either original or newly created) that may help to restrict interparticle sliding and rotation. This second mechanism tends to cause dilation for a granular body (Fig. 19(c)). The two mechanisms manifest the relative dominance of evolving grain size and changing grain shape during their intertwined evolution and affect characteristic states of crushable sand in different manners.

The concept of critical state has been the cornerstone of critical state theory and modern critical state soil mechanics. Although there have been extensive studies claiming the identification of critical state in crushable sand, some critical questions still need to be carefully answered. (a) In addition to conditions of constant volume and constant stresses, are there additional conditions needed to define the critical state in crushable sand? (b) Will grain crushing totally cease to occur at critical state or will it reach a somehow constant steady-state crushing rate? (c) How would the overall grain shape characteristics evolve to a critical state? (d) How will fabric anisotropy behave at the critical state for crushable sand? Question (b) is probably among the most intriguing ones to explore. It is anticipated that a fractal limit with no further crushing events occurring can only possibly be reached asymptotically under favourable loading modes (e.g. 1D compression, as shown in Zhu & Zhao (2019a)).

In general loading conditions, a dynamically balanced state can possibly be attained, featured with a steady, low crushing rate, to allow all other critical state conditions to be satisfied according to our classic understanding of it. If this conjecture is true, it is indeed possible to employ the two competing mechanisms proposed above to offer a possible interpretation as follows. At critical state with a steady crushing rate, the void-filling-induced volumetric contraction cancels out the dilation induced by interparticle friction and interlocking with increased shape complexity, leading to a constant volume state for crushable sand. From the perspective of mechanical balance, the cushioning effect with increasing small particles generated may tend to homogenise a specimen to lower its loading bearing capacity; meanwhile, the shape-induced friction and interlocking may help to enhance the strength of sand. At critical state, the two mechanical mechanisms reach a balance to allow constant stresses. The same explanation may be applicable for fabric anisotropy, where smaller grains will make a specimen more isotropic and shape effects induced by the new shapes created tend to enhance anisotropy. The two mechanisms reach a balance at the critical state to allow a constant anisotropy to be identified.

The above conjecture, however, needs rigorous experimental and numerical evidence. In this study, when the simulation specimens are sheared under a relatively low confining pressure of  $\sigma_3 = 1.5$  MPa, a steady state with constant stress and volume is reached at an axial strain in excess of 60% (Fig. 5). Nonetheless, this steady state is still marked by continuous particle breakage with a steady growth of Hardin's breakage index (Fig. 7). If such a state is regarded as close to the critical state, it appears to support the dynamically balanced conjecture with the steady crushing rate mentioned above. However, other simulation cases under higher confining pressures exhibit a strongly contractive behaviour, with considerable breakage events sustained even at large axial strain over 60%. Their inability to achieve a constant volume condition indicates a critical state has not been reached. Future experimental tests and numerical modelling must be designed to allow excessively large shear deformation to be developed. It is also important that any numerical approaches should try to minimise assumptions or constraints on both grain size and grain shape changes during crushing to render a critical state to be reached in a more natural and realistic manner.

Before the critical state is reached, the dilatancy behaviour of crushing sand is closely related to its state (e.g. initial density and pressure) and loading path. While this study is focused on exploring the influence of confining pressure and intermediate principal stress ratio on the shear deformation of crushable sand, the influence of initial relative density has not been systematically examined. All initial specimens prior to shearing have been consolidated to dense packings to facilitate crushing, which can be confirmed by the dominantly dilative behaviour shown by the non-crushable comparison cases. Nevertheless, different combinations of relative density, mean stress and loading path (e.g. variable  $b$  conditions) may control the grain crushing rate and the evolution rate of grain shape differently, manifesting different dilatancy behaviours for crushable sand. Take the  $b = 0.0$  and  $\sigma_3 = 5.0$  MPa case in Fig. 5(b) as an example. The transition of volumetric strain from dilative to contractive is interesting, as it is contradictory to common observations on sand. Under this median confining pressure, the shape effects of new child particles created during the initial stage crushing events in conjunction with the dense initial packing cause the overall dilative responses of the specimen. With further shearing and more small particles being generated, the void-filling mechanism begins to overtake the other factors

and leads to prevalingly contractive behaviour at large shear strain. Higher confining pressure may cause an earlier and higher rate of crushing events that may push the dominance of the void-filling mechanism to occur earlier. For extremely high confining cases such as  $\sigma_3 = 12$  MPa, this happens from the very beginning of the shearing. Note that the crushing rate and evolution rate of shape are not synchronised and indeed they change at different speeds. Under high confining pressure, the crushing rate remains positive when the particle shape almost ceases to evolve and reaches a relatively stable state after 30% axial strain (Figs 8 and 9). Consequently, the dilative responses brought by resistance and interlocking of irregular particles are gradually outweighed by the contraction induced from fine particles filling pores under a steady crushing rate. This indicates that the void-filling effect appears to be a crucial factor in controlling the deformation of crushable sand under elevated stress conditions, contributing to a transition from volumetric dilation to contraction.

## CONCLUSIONS

This study presents a comprehensive investigation of the behaviour of crushable granular sand under general stress conditions based on numerical simulations using a hybrid PD and NSCD approach. The hybrid PD–NSCD method offers rigorous consideration of the co-evolution of both grain size and grain shape during a typical crushing process and provides a physics-based tool for quantitative analysis of grain breakage in granular media. Numerical simulations were performed for crushable granular sand subjected to true triaxial shear under different confining stresses and intermediate principal stress ratios. A systematic examination of the numerical results helps to establish correlations between the macroscopic properties of crushable sand and their microstructural origins. It enables a better understanding on various aspects of crushing sand, including the strength, deformability, particle size and shape evolution, particle-scale contact anisotropy and force transmission. It also offers new data for corroborating with continuum models developed for crushable granular media (such as the recent one by Buscarnera & Einav (2021)). Major findings from the study are summarised as follows.

- (a) The strength and deformation of crushable granular sand depend closely on the intermediate stress ratio  $b$ . The present study shows the mobilised friction angle of crushable sand reaches a peak value at around  $b = 0.5$ . Under otherwise identical conditions, increasing  $b$  causes more significant particle crushing due to increased mean confinements, leading to a more poly-dispersed gradation and possibly a gradual transition of deformation mode from dilation to contraction.
- (b) Particle crushing is found to sustain up to large shear strain levels (over 60% of axial strain) with a nearly constant increasing rate for the Hardin's breakage index under all loading conditions. At higher  $b$  conditions, particle size evolves towards a fractal distribution with a higher fractal dimension and shows a stronger 'cushioning effect'. Particle shape distribution evolves with particle crushing towards a steady-state profile, and such profile does not appear to be affected by  $b$ . Whether or not the steady state is unique, however, needs further investigations.
- (c) The crushing pattern of particles in terms of the number of child particles is revealed to be an intrinsic material property that is independent of stress conditions. The influence of contact forces on particle crushability,

especially strong contact forces controlled by the intermediate principal stress ratio, dictates over other factors, such as size, shape and coordination number, during the crushing process.

- (d) The present micromechanical study shows that the dependency of shear strength on  $b$  arises from a combined effect of decreased number of original particles and newly formed child particles participating in the strong force chains. Shear-induced contact normal anisotropy is provided by child particles from both the strong and weak contact force subnetworks.

The findings from this study aggregate existing knowledge on the roles of the intermediate principal stress ratio to deepen understanding of the behaviour of crushable granular materials. Future improvements are expected to be made on the following aspects. (a) Better design for both numerical and experimental studies is needed to allow extremely high shear strain if the critical state of crushable sand is the focus. The current study shows that a general critical state has not been reached for highly crushable sands in general stress conditions, even though the specimen is sheared to over 60% axial strain. (b) In addition to constant  $b$  tests, other testing conditions, such as undrained shear and constant  $p$ , can be examined to corroborate existing findings and offer a more comprehensive understanding of crushable granular media. (c) A quantitative analysis is required to elucidate the competing roles played by two dominant mechanisms on the deformation behaviour of crushable sand, the enhanced void filling driven by increasing finer grain size that tends to cause contraction and the mobilised friction and interlocking enhanced by changing grain shape that favours dilation. How the relevant dominance of the two mechanisms may play out under different soil states and stress conditions needs further quantitative study.

## ACKNOWLEDGEMENTS

This study was financially supported by the National Natural Science Foundation of China (under project 11972030) and the Research Grants Council of Hong Kong (GRF #16208720). The first author acknowledges financial support from the Hong Kong PhD Fellowship Scheme funded by the Research Grants Council of Hong Kong.

## NOTATION

$A_c$	contact normal anisotropy
$A_p$	surface area of a particle
$b$	intermediate principal stress ratio
$\mathbf{b}$	body force density
$\mathbf{D}_{i,n}, \mathbf{D}_{i,u}, \mathbf{D}_{i,w}$	normal and tangential contact vectors
$d$	particle diameter
$d_j^c$	branch vector at contact $c$ in direction $j$
$\mathbf{f}, \mathbf{g}_q$	external force and constraint force
$f_i^c$	contact force at contact $c$ in direction $i$
$f_n$	mean contact force
$G_c$	critical energy release rate
$H$	height of a sample
$I_m$	inertia number
$\mathbf{M}, \mathbf{v}$	mass and velocity of objects in contact
$N_c$	number of contacts
$N_p$	number of particles excluding rattlers
$\mathbf{n}$	unit vector along contact normal direction
$p_0$	confining pressure
$p'$	mean effective stress
$q$	deviator stress
$\mathbf{q}$	generalised particle position
$\dot{\mathbf{q}}$	derivative of particle position
$S, K$	shear and bulk modulus

$s_c$	critical stretch
$T$	peridynamic force state
$\mathbf{u}$	displacement vector
$\ddot{\mathbf{u}}$	acceleration
$V$	volume of a particle
$V_x$	volume of a material point
$Z_m$	coordination number
$\perp$	orthogonality
$\delta$	horizon
$\gamma_{i,n}, \gamma_{i,u}, \gamma_{i,w}$	normal and tangential contact force of contact $i$
$\epsilon_1$	axial strain
$\dot{\epsilon}_1$	axial strain rate
$\epsilon_v$	volumetric strain
$\eta$	stress ratio
$\mu$	inter-particle friction coefficient
$\rho$	material density
$\sigma_1, \sigma_2, \sigma_3$	principal stress components
$\sigma_{ij}$	stress tensor
$\sigma_{ij}^d$	deviatoric part of stress tensor
$\Phi_{ij}$	fabric tensor
$\Phi_{ij}^d$	deviatoric part of fabric tensor
$\phi_i$	contact distance
$\phi_m$	angle of shearing resistance
$\Psi$	sphericity
$\psi$	Weibull modulus
$\Omega_x$	family of a material point $x$

## REFERENCES

- Anitescu, M. & Tasora, A. (2010). An iterative approach for cone complementarity problems for nonsmooth dynamics. *Comput. Optim. Appl.* **47**, No. 2, 207–235.
- ASTM (2011). D 7181: Method for consolidated drained triaxial compression test for soils, Annual book of standards, vol. 4, pp. 1–11. West Conshohocken, PA, USA: ASTM International.
- Bandini, V. & Coop, M. R. (2011). The influence of particle breakage on the location of the critical state line of sands. *Soils Found.* **51**, No. 4, 591–600.
- Buscarnera, G. & Einav, I. (2021). The mechanics of brittle granular materials with coevolving grain size and shape. *Proc. R. Soc. A* **477**, No. 2249, 20201005.
- Christoffersen, J., Mehrabadi, M. M. & Nemat-Nasser, S. (1981). A micromechanical description of granular material behavior. *J. Appl. Mech.* **48**, No. 2, 339–344.
- Ciantia, M. O., Arroyo, M., Calvetti, F. & Gens, A. (2015). An approach to enhance efficiency of DEM modelling of soils with crushable grains. *Géotechnique* **65**, No. 2, 91–110, <https://doi.org/10.1680/geot.13.P218>.
- Ciantia, M. O., Arroyo, M., O'Sullivan, C. & Gens, A. (2019). Micromechanical inspection of incremental behaviour of crushable soils. *Acta Geotech.* **14**, No. 5, 1337–1356.
- Coop, M. R., Sorensen, K. K., Bodas Freitas, T. & Georgoutsos, G. (2004). Particle breakage during shearing of a carbonate sand. *Géotechnique* **54**, No. 3, 157–163, <https://doi.org/10.1680/geot.2004.54.3.157>.
- De Bono, J. P. & McDowell, G. R. (2018). Micro mechanics of drained and undrained shearing of compacted and overconsolidated crushable sand. *Géotechnique* **68**, No. 7, 575–589, <https://doi.org/10.1680/jgeot.16.P318>.
- Domokos, G., Kun, F., Sipos, A. A. & Szabó, T. (2015). Universality of fragment shapes. *Sci. Rep.* **5**, No. 1, 1–6.
- Fabri, A. & Pion, S. (2009). CGAL: The computational geometry algorithms library. In *Proceedings of the 17th ACM SIGSPATIAL international conference on advances in geographic information systems* (eds D. Agrawal, W. G. Aref, C.-T. Lu, M. F. Mokbel, P. Scheuermann, C. Shahabi and O. Wolfson), pp. 538–539. New York, NY, USA: Association for Computing Machinery.
- Guo, N. & Zhao, J. (2013). The signature of shear-induced anisotropy in granular media. *Comput. Geotech.* **47**, 1–15.
- Hanley, K. J., O'Sullivan, C. & Huang, X. (2015). Particle-scale mechanics of sand crushing in compression and shearing using DEM. *Soils Found.* **55**, No. 5, 1100–1112.
- Hardin, B. O. (1985). Crushing of soil particles. *J. Geotech. Engng* **111**, No. 10, 1177–1192.
- Huang, X., Hanley, K. J., O'Sullivan, C., Kwok, C. Y. & Wadee, M. A. (2014a). DEM analysis of the influence of the intermediate stress ratio on the critical-state behaviour of granular materials. *Granul. Matter* **16**, No. 5, 641–655.
- Huang, X., Hanley, K. J., O'Sullivan, C. & Kwok, C. Y. (2014b). Exploring the influence of interparticle friction on critical state behaviour using DEM. *Int. J. Numer. Analyt. Methods Geomech.* **38**, No. 12, 1276–1297.
- Hurley, R. C., Lind, J., Pagan, D. C., Akin, M. C. & Herbold, E. B. (2018). In situ grain fracture mechanics during uniaxial compaction of granular solids. *J. Mech. Phys. Solids* **112**, 273–290.
- Izadi, E. & Bezuijen, A. (2018). Simulating direct shear tests with the bullet physics library: a validation study. *PLoS One* **13**, No. 4, e0195073.
- Jean, M. (1999). The non-smooth contact dynamics method. *Comput. Methods Appl. Mech. Engng* **177**, No. 3–4, 235–257.
- Jia, Y., Xu, B., Chi, S., Xiang, B. & Zhou, Y. (2017). Research on the particle breakage of rockfill materials during triaxial tests. *Int. J. Geomech.* **17**, No. 10, 04017085.
- Karatza, Z., Ando, E., Papanicolopoulos, S. A., Ooi, J. Y. & Viggiani, G. (2018). Evolution of deformation and breakage in sand studied using X-ray tomography. *Géotechnique* **68**, No. 2, 107–117, <https://doi.org/10.1680/jgeot.16.P208>.
- Karatza, Z., Ando, E., Papanicolopoulos, S., Viggiani, G. & Ooi, J. Y. (2019). Effect of particle morphology and contacts on particle breakage in a granular assembly studied using X-ray tomography. *Granul. Matter* **21**, No. 3, 1–13.
- Kendall, K. (1978). The impossibility of comminuting small particles by compression. *Nature* **272**, No. 5655, 710–711.
- Kleinert, J., Obermayr, M. & Balzer, M. (2013). Modeling of large scale granular systems using the discrete element method and the non-smooth contact dynamics method: a comparison case study. *ECCOMAS multibody dynamics conference*, Zagreb, Croatia.
- Köken, E. (2020). Evaluation of size reduction process for rock aggregates in cone crusher. *Bull. Engng Geol. Environ.* **79**, No. 9, 4933–4946.
- Kopta, D., Ize, T., Spjut, J., Brunvand, E., Davis, A. & Kensler, A. (2012). Fast, effective BVH updates for animated scenes. In *Proceedings of the ACM SIGGRAPH symposium on interactive 3D graphics and games* (ed. S. N. Spencer), pp. 197–204. New York, NY, USA: Association for Computing Machinery.
- Kwasniewski, M., Li, X. & Takahashi, M. (2012). *True triaxial testing of rocks*. Boca Raton, FL, USA: CRC Press.
- Lade, P. V., Yamamoto, J. A. & Bopp, P. A. (1996). Significance of particle crushing in granular materials. *J. Geotech. Engng* **122**, No. 4, 309–316.
- Lin, L., Li, S., Sun, L., Liu, X. & Chen, W. (2020). Evolution of particle size distribution for carbonate sand under impact load. *Powder Technol.* **376**, 549–545.
- Liu, Y., Liu, H. & Mao, H. (2017). DEM investigation of the effect of intermediate principal stress on particle breakage of granular materials. *Comput. Geotech.* **84**, 58–67.
- Lobo-Guerrero, S. & Vallejo, L. E. (2005). Crushing a weak granular material: experimental numerical analyses. *Géotechnique* **55**, No. 3, 245–249, <https://doi.org/10.1680/geot.2005.55.3.245>.
- Luding, S., Clément, E., Blumen, A., Rajchenbach, J. & Duran, J. (1994). Studies of columns of beads under external vibrations. *Phys. Rev. E* **49**, No. 2, 1634–1646.
- Luzzani, L. & Coop, M. R. (2002). On the relationship between particle breakage and the critical state of sands. *Soils Found.* **42**, No. 2, 71–82.
- Madenci, E. & Oterkus, E. (2014). *Peridynamic theory and its applications*. New York, NY, USA: Springer.
- McDowell, G. R. (2002). On the yielding and plastic compression of sand. *Soils Found.* **42**, No. 1, 139–145.
- McDowell, G. R. & de Bono, J. P. (2013). On the micro mechanics of one-dimensional normal compression. *Géotechnique* **63**, No. 11, 895–908, <https://doi.org/10.1680/geot.12.P041>.
- Melanz, D. J. (2016). *Physics-based contact using the complementarity approach for discrete element applications in vehicle mobility and terramechanics*. Madison, WI, USA: The University of Wisconsin.
- Miao, G. & Airey, D. (2013). Breakage and ultimate states for a carbonate sand. *Géotechnique* **63**, No. 14, 1221–1229, <https://doi.org/10.1680/geot.12.P111>.

- Nakata, A., Hyde, M., Hyodo, H. & Murata (1999). A probabilistic approach to sand particle crushing in the triaxial test. *Géotechnique* **49**, No. 5, 567–583, <https://doi.org/10.1680/geot.1999.49.5.567>.
- Nakata, Y., Hyodo, M., Hyde, A. F., Kato, Y. & Murata, H. (2001). Microscopic particle crushing of sand subjected to high pressure one-dimensional compression. *Soils Found.* **41**, No. 1, 69–82.
- Nguyen, D., Azéma, E., Sornay, P. & Radjai, F. (2018). Rheology of granular materials composed of crushable particles. *Eur. Phys. J. E: Soft Matter Biol. Phys.* **41**, No. 4, article 50.
- Oda, M. & Iwashita, K. E. (2020). *Mechanics of granular materials: an introduction*. Boca Raton, FL, USA: CRC Press.
- Parks, M. L., Littlewood, D. J., Mitchell, J. A. & Silling, S. A. (2012). *Peridigm users' guide v1. 0.0*, SAND Report 7800. Albuquerque, NM and Livermore, CA, USA: Sandia National Laboratories.
- Perez, J. L., Kwok, C. Y., Huang, X. & Hanley, K. J. (2016). Assessing the quasi-static conditions for shearing in granular media within the critical state soil mechanics framework. *Soils Found.* **56**, No. 1, 152–159.
- Radjai, F., Wolf, D. E., Jean, M. & Moreau, J. (1998). Bimodal character of stress transmission in granular packings. *Phys. Rev. Lett.* **80**, No. 1, 61–64.
- Rothenburg, L. & Bathurst, R. J. (1989). Analytical study of induced anisotropy in idealized granular materials. *Géotechnique* **39**, No. 4, 601–614, <https://doi.org/10.1680/geot.1989.39.4.601>.
- Sazzad, M. M. & Suzuki, K. (2013). Density dependent macro-micro behavior of granular materials in general triaxial loading for varying intermediate principal stress using DEM. *Granul. Matter* **15**, No. 5, 583–593.
- Servin, M., Wang, D., Lacoursière, C. & Bodin, K. (2014). Examining the smooth and nonsmooth discrete element approaches to granular matter. *Int. J. Numer. Methods Engng* **97**, No. 12, 878–902.
- Silling, S. A., Epton, M., Weckner, O., Xu, J. & Askari, E. (2007). Peridynamic states and constitutive modeling. *J. Elast.* **88**, No. 2, 151–184.
- Tasora, A., Serban, R., Mazhar, H., Pazouki, A., Melanz, D., Fleischmann, J., Taylor, M., Sugiyama, H. & Negrut, D. (2015). Chrono: an open source multi-physics dynamics engine. In *High performance computing in science and engineering: second international conference, HPCSE 2015, Solan, Czech Republic, May 25–28, 2015, revised selected papers* (eds T. Kozubek, R. Blaheta, J. Sistek, M. Rozložnik and M. Čermák), pp. 19–49. Cham, Switzerland: Springer International.
- Thornton, C. (1979). The conditions for failure of a face-centered cubic array of uniform rigid spheres. *Géotechnique* **29**, No. 4, 441–459, <https://doi.org/10.1680/geot.1979.29.4.441>.
- Tsounqui, O., Vallet, D. & Charmet, J. (1999). Numerical model of crushing of grains inside two-dimensional granular materials. *Powder Technol.* **105**, No. 1–3, 190–198.
- Van den Bergen, G. (2003). *Collision detection in interactive 3D environments*. Boca Raton, FL, USA: CRC Press.
- Wang, Q. & Lade, P. V. (2001). Shear banding in true triaxial tests and its effect on failure in sand. *J. Engng Mech.* **127**, No. 8, 754–761.
- Wang, J. & Yan, H. (2012). DEM analysis of energy dissipation in crushable soils. *Soils Found.* **52**, No. 4, 644–657.
- Wang, J. & Yan, H. (2013). On the role of particle breakage in the shear failure behavior of granular soils by DEM. *Int. J. Numer. Analyt. Methods Geomech.* **37**, No. 8, 832–854.
- Wei, H., Yin, M., Zhao, T., Yan, K., Shen, J., Meng, Q., Wang, X. & He, J. (2021). Effect of particle breakage on the shear strength of calcareous sands. *Mar. Geophys. Res.* **42**, No. 3, article 23.
- Xiao, Y., Liu, H., Chen, Y. & Chu, J. (2014). Influence of intermediate principal stress on the strength and dilatancy behavior of rockfill material. *J. Geotech. Geoenviron. Engng* **140**, No. 11, 04014064.
- Xiao, Y., Sun, Y., Liu, H. & Yin, F. (2016). Critical state behaviors of a coarse granular soil under generalized stress conditions. *Granul. Matter* **18**, No. 2, article 17.
- Yu, F. (2017a). Stress–dilatancy behavior of sand incorporating particle breakage. *Acta Geotech. Slovenica* **14**, No. 1, 55–61.
- Yu, F. (2017b). Particle breakage and the drained shear behavior of sands. *Int. J. Geomech.* **17**, No. 8, 04017041.
- Yu, F. (2017c). Characteristics of particle breakage of sand in triaxial shear. *Powder Technol.* **320**, 656–667.
- Zhao, B., Wang, J., Coop, M. R., Viggiani, G. & Jiang, M. (2015). An investigation of single sand particle fracture using X-ray micro-tomography. *Géotechnique* **65**, No. 8, 625–641, <https://doi.org/10.1680/geot.4.P157>.
- Zhong, W., Yue, F. & Ciancio, A. (2018). Fractal behavior of particle size distribution in the rare earth tailings crushing process under high stress condition. *Appl. Sci.* **8**, No. 7, 1058.
- Zhou, W., Yang, L., Ma, G., Chang, X., Cheng, Y. & Li, D. (2015). Macro–micro responses of crushable granular materials in simulated true triaxial tests. *Granul. Matter* **17**, No. 4, 497–509.
- Zhu, F. & Zhao, J. (2019a). Modeling continuous grain crushing in granular media: a hybrid peridynamics and physics engine approach. *Comput. Methods Appl. Mech. Engng* **348**, 334–355.
- Zhu, F. & Zhao, J. (2019b). A peridynamic investigation on crushing of sand particles. *Géotechnique* **69**, No. 6, 526–540, <https://doi.org/10.1680/jgeot.17.P274>.
- Zhu, F. & Zhao, J. (2021a). Multiscale modeling of continuous crushing of granular media: the role of grain microstructure. *Computational Particle Mechanics* **8**, No. 5, 1089–1101.
- Zhu, F. & Zhao, J. (2021b). Interplays between particle shape and particle breakage in confined continuous crushing of granular media. *Powder Technol.* **378**, 455–467.